

# A new diagnostic for AMOC heat transport applied to the CESM large ensemble

C Spencer Jones<sup>1</sup>, Scout Jiang<sup>2</sup>, and Ryan Abernathey<sup>2</sup>

<sup>1</sup>Texas A&M University

<sup>2</sup>Columbia University

August 24, 2023

## Abstract

Atlantic time-mean heat transport is northward at all latitudes and exhibits strong multidecadal variability between about 30N and 55N. Atlantic heat transport variability influences many aspects of the climate system, including regional surface temperatures, subpolar heat content, Arctic sea-ice concentration and tropical precipitation patterns. Atlantic heat transport and heat transport variability are commonly partitioned into two components: the heat transport by the AMOC and the heat transport by the gyres. In this paper we compare three different methods for performing this partition, and we apply these methods to the CESM1 Large Ensemble at 34N, 26N and 5S. We discuss the strengths and weaknesses of each method. One of these methods is a new physically-motivated method based on the pathway of the northward-flowing part of AMOC. This paper presents a preliminary version of our method. This preliminary version works only when the AMOC follows the western boundary of the basin. In this context, the new method provides a sensible estimate of heat transport by the overturning and by the gyre, and it is easier to interpret than other methods. According to our new diagnostic, at 34N and at 26N AMOC explains 120% of the multidecadal variability (20% is compensated by the gyre), and at 5S AMOC explains 90% of multidecadal variability.

1 **A new diagnostic for AMOC heat transport applied to**  
2 **the CESM large ensemble**

3 **C Spencer Jones<sup>1</sup>, Scout Jiang<sup>2</sup> and Ryan P. Abernathey<sup>2</sup>**

4 <sup>1</sup>Texas A&M University, College Station, TX

5 <sup>2</sup>Columbia University, New York, NY

6 **Key Points:**

- 7 • We introduce a new diagnostic for AMOC heat transport that partitions the flow  
8 into mass-conserving gyre and overturning components
- 9 • The new method is compared with the standard method that relies on zonally av-  
10 eraging the temperature and velocity fields
- 11 • The new method provides a clearer way of separating heat transport by the gyres  
12 and by the overturning

---

Corresponding author: C. Spencer Jones, [spencerjones@tamu.edu](mailto:spencerjones@tamu.edu)

**Abstract**

Atlantic time-mean heat transport is northward at all latitudes and exhibits strong multidecadal variability between about 30°N and 55°N. Atlantic heat transport variability influences many aspects of the climate system, including regional surface temperatures, subpolar heat content, Arctic sea-ice concentration and tropical precipitation patterns. Atlantic heat transport and heat transport variability are commonly partitioned into two components: the heat transport by the AMOC and the heat transport by the gyres. In this paper we compare three different methods for performing this partition, and we apply these methods to the CESM1 Large Ensemble at 34°N, 26°N and 5°S. We discuss the strengths and weaknesses of each method. One of these methods is a new physically-motivated method based on the pathway of the northward-flowing part of AMOC. This paper presents a preliminary version of our method. This preliminary version works only when the AMOC follows the western boundary of the basin. In this context, the new method provides a sensible estimate of heat transport by the overturning and by the gyre, and it is easier to interpret than other methods. According to our new diagnostic, at 34°N and at 26°N AMOC explains 120% of the multidecadal variability (20% is compensated by the gyre), and at 5°S AMOC explains 90% of multidecadal variability.

**Plain Language Summary**

Scientists often want to quantify how much heat is transported by the Atlantic Meridional Overturning Circulation (sometimes called the “Conveyor Belt” circulation) and how much heat is transported by the ocean’s gyres. This paper compares some different methods for estimating the heat transport by the overturning circulation and by the gyres, including a new method that has not been used before. While previous methods are easier to apply to observations, the new method gives results that are easier to understand.

**1 Introduction**

The Atlantic Meridional Overturning Circulation (AMOC) comprises northward flow of warmer water near the surface, deep water formation in the North Atlantic, and southward flow of cooler water at depth. The AMOC transports heat northward throughout the Atlantic basin, warming the Northern Hemisphere (Jackson et al., 2015; Buckley & Marshall, 2016) and performing 20% of the total planetary poleward heat trans-

44 port at 26.5°N (Trenberth & Fasullo, 2017). The AMOC’s cross-equatorial heat trans-  
45 port shifts the intertropical convergence zone (ITCZ) northward, affecting precipitation  
46 patterns close to the equator (Kang et al., 2009; Marshall et al., 2014).

47 Variations in northward Atlantic heat transport are thought to be a key driver of  
48 Atlantic Multidecadal Variability (Oldenburg et al., 2021), which affects variability in mul-  
49 tiple parts of the climate system (Zhang et al., 2019), including tropical precipitation  
50 (Folland et al., 1986; Martin & Thorncroft, 2014), Atlantic hurricane frequency (Goldenberg  
51 et al., 2001; Klotzbach et al., 2015), and North Atlantic sea ice variability (Yeager et al.,  
52 2015). Low frequency ocean variability is a source of predictability in the climate sys-  
53 tem, meaning that parts of the climate system that are driven by AMOC variability may  
54 be predictable using observations of the ocean (Borchert et al., 2018). AMOC low-frequency  
55 variability and Atlantic decadal predictability vary significantly between climate mod-  
56 els (Yan et al., 2018). To understand the cause of differences between models, it is help-  
57 ful to characterize how the AMOC and the gyres interact to influence northward ocean  
58 heat transport. In this paper, we use three different methods to estimate how much ocean  
59 heat transport is performed by AMOC.

60 Many studies have attempted to separate the heat transport by the overturning  
61 circulation from the heat transport by the gyres (e.g. Bryan (1962); Hall and Bryden  
62 (1982); McDonagh et al. (2010); Ferrari and Ferreira (2011); Piecuch et al. (2017)). Most  
63 studies suggest that AMOC is the primary driver of heat transport in the subtropical  
64 gyre region and that the gyre is a more important driver in the subpolar gyre region (Eden  
65 & Willebrand, 2001; Piecuch et al., 2017). Many of the studies that have partitioned the  
66 heat transport by the gyres and the heat transport by the overturning circulation have  
67 done so with the goal of identifying how much of the heat transport variability is driven  
68 by wind and how much is driven by buoyancy forcing. AMOC variability is often thought  
69 to be primarily driven by buoyancy forcing, and the gyres are thought to be primarily  
70 driven by wind forcing. But recent studies have shown that gyre strength is strongly in-  
71 fluenced by buoyancy forcing (Bhagtani et al., 2023), and that AMOC strength is strongly  
72 influenced by wind forcing (Yang, 2015; Cessi, 2018). The goal of this study is not to par-  
73 tition the heat transport caused by wind from the heat transport caused by buoyancy  
74 forcing, but to elucidate how the total AMOC transport influences heat transport at mul-  
75 tiple latitudes, and to clarify whether this heat transport takes place on the western bound-  
76 ary or in the interior of the basin.

77 Most previous studies define the heat transport by the overturning as the zonal in-  
78 tegral of the volume transport multiplied by the zonal mean temperature, integrated in  
79 the vertical. In all the studies that use this method, the integrals are taken in depth space.  
80 In the last twenty years or so, oceanographers have started to define the AMOC using  
81 a zonal-average in density space (Foukal & Chafik, 2022). Recent work by Zhang and  
82 Thomas (2021) has shown that flows on the same depth level in the subpolar gyre re-  
83 gion have different densities and form part of the AMOC. It is clear that the old depth-  
84 averaged way of looking at things can still be useful, but much progress has been made  
85 by looking at the AMOC in new ways.

86 In this work, we introduce a new method for partitioning the heat transport due  
87 to the overturning and the heat transport due to the gyres based on a more nuanced un-  
88 derstanding of the circulation patterns. Northward flow in the North Atlantic is dom-  
89 inated by the Gulf Stream. The Gulf Stream is significantly stronger than required to  
90 satisfy Sverdrup balance (Gray & Riser, 2014), which can partly be attributed to the pres-  
91 ence of an additional flow component: the northward component of the AMOC. AMOC  
92 transport primarily follows the western boundary at latitudes where the gyre is clock-  
93 wise (Stommel, 1957). Rypina et al. (2011) showed that drifters in the far west of the  
94 Gulf Stream are likely to reach the North Atlantic, whereas drifters further to the east  
95 are unlikely to cross northward into latitudes associated with the subpolar gyre. In this  
96 work we extend this idea, splitting the upper part of the ocean into AMOC transport,  
97 which follows the western boundary, and gyre transport, which occupies the interior.

98 Our method is conceptually similar to a method used by Roemmich and Wunsch  
99 (1985). Roemmich and Wunsch (1985) estimated the temperature transport in the deep  
100 ocean, the temperature transport in the western boundary current, and the temperature  
101 transport in the southward flowing part of the gyre from observations. Talley (1999) used  
102 a similar method. These authors took the mean temperature in the western boundary  
103 current and calculated the heat transport by the AMOC to be the volume transport of  
104 the AMOC multiplied the difference in temperature between the western boundary cur-  
105 rent and the deep ocean. They applied their method to sections at 24°N and found that  
106 90% of the mean northward heat transport is performed by the AMOC at this latitude,  
107 and they commented that the northward heat transport is dominated by the AMOC across  
108 multiple years of observations. Because our new method is applied to a model, we are  
109 able to more clearly define the regions associated with the AMOC and with the gyre.

110 In this work, we compare three methods for partitioning ocean heat transport into  
111 heat transport by the overturning and heat transport by the gyres. We use the CESM  
112 large ensemble as a testbed for these different methods, because the existence of long runs  
113 and many ensemble members allows us to examine variability at multiple timescales. The  
114 CESM large ensemble is described in section 2 and the three methods for partitioning  
115 heat transport by the overturning and heat transport by the gyres are described in sec-  
116 tion 2.1. Sections 3.1 and 3.2 describe the total AMOC and heat transport variability  
117 in the CESM large ensemble, and section 3.3 shows the results of different methods for  
118 partitioning the heat transport by the overturning and the heat transport by the gyres.  
119 Section 4 discusses the results and presents conclusions.

## 120 **2 Methods**

121 We explore these diagnostics in the context of ocean models, where the time vary-  
122 ing circulation and temperature fields are perfectly known. Our analysis uses a large en-  
123 semble of ocean simulation in order to sample broadly the modes of natural variability  
124 of the North Atlantic circulation. The CESM Large Ensemble is a group of simulations  
125 performed using a  $1^\circ$  nominal resolution fully-coupled version of the Community Earth  
126 System Model (CESM1) (Kay et al., 2015). Forty ensemble members were created for  
127 the period 1920-2100. Each ensemble member has the same radiative forcing scenario,  
128 but the initial atmospheric temperature is perturbed with a spatially random perturba-  
129 tion order  $10^{-14}$ K. As a result of internal variability, each ensemble member’s state fol-  
130 lows a unique trajectory with different regional temperature patterns and different AMOC  
131 variability.

132 We used the cloud-optimized dataset, which is stored on Amazon Web Services (AWS)  
133 thanks to the AWS Public Dataset Program (de La Beaujardiere et al., 2019). In this  
134 work we used the first 35 ensemble members for the period 1940-2005. 1940 is chosen  
135 because this allows time for the internal variability of the system to diverge, so that the  
136 ensemble members are different from each other throughout the chosen period. 2005 is  
137 a natural end date, because it marks the end of the historical runs for the CESM1 Large  
138 Ensemble. During the period 1940-2005 multidecadal variability dominates over long-  
139 term trends in AMOC and heat transport. Members of the CESM large ensemble are  
140 not meant to have exactly the same variability as the real world, but to represent the  
141 range of possible internal variability. Many of the ensemble members exhibit North At-

142 lantic subpolar gyre ocean heat content variability with similar magnitude to ECCOv4r3  
 143 (not shown).

## 144 **2.1 Separating heat transport by the gyre from heat transport by the** 145 **overturning circulation**

146 Heat transport by each gyre is primarily wind driven, and is likely to have short  
 147 time scales and spatial effects that are confined to that gyre. Heat transport by the over-  
 148 turning is both wind and buoyancy driven, and is more likely to impact temperatures  
 149 in the far North Atlantic. Hence, it is desirable to partition the heat transport across  
 150 a particular latitude into the heat transport by the overturning and the heat transport  
 151 by the gyres. All the methods described in this section are designed to be applied at a  
 152 fixed latitude. The notion of heat transport by the flow across a section is only well-defined  
 153 when the net mass transport (or volume transport, in a Boussinesq ocean model) of the  
 154 flow is zero (see e.g. Warren (1999); Boccaletti et al. (2005); Pickart and Spall (2007)).  
 155 In the Atlantic basin, there is a net southward volume transport of about 1 Sv, and the  
 156 heat transported by this net throughflow is dependent on our choice of reference tem-  
 157 perature. We still remove the net throughflow component of the heat transport. Because  
 158 the net throughflow is small, the results of this study are relatively insensitive to the choice  
 159 of reference temperature.

160 At each latitude, we remove the mean velocity from the total velocity to find the  
 161 volume conserving part of the velocity,

$$v_{vc}(x, z, t) = v(x, z, t) - \bar{v}(t), \quad (1)$$

162 where

$$\bar{v}(t) = \frac{\int_{-H}^0 \int_{x_w}^{x_e} v(x, z, t) dx dz}{\int_{-H}^0 \int_{x_w}^{x_e} dx dz}, \quad (2)$$

163 and  $x$  is distance in the longitudinal direction,  $z$  is distance in the vertical,  $v$  is the merid-  
 164 ional velocity,  $H$  is the ocean depth,  $x_w$  is the western boundary of the Atlantic and  $x_e$   
 165 is the eastern boundary of the Atlantic. Ideally, the residual velocity (including the eddy  
 166 transport) would be used in these calculations, but this data was not readily available,  
 167 so the effects of parameterized eddies are not included in  $v$ . We also remove the south-  
 168 ward heat transport that is associated with the mean velocity, so

$$\text{OHT}_{vc}(t) = \int_{-H}^0 \int_{x_w}^{x_e} v(x, z, t) \theta(x, z, t) dx dz - \int_{-H}^0 \int_{x_w}^{x_e} \theta(x, z, t) \bar{v}(t) dx dz, \quad (3)$$

169 where  $\theta$  is temperature.

170 The total volume conserving heat transport,  $\text{OHT}_{vc}$ , can be further decomposed  
 171 into the sum of heat transport by multiple sub-flows, provided that each sub-flow has  
 172 no net mass transport associated with it. There are infinitely many possible such decom-  
 173 positions. Once the net velocity and associated heat transport have been removed, we  
 174 apply and compare three methods for separating the heat transport by the overturning  
 175 and the heat transport by the gyres. These methods are illustrated in figure 1. The first  
 176 method, which we call the zonal-mean method in  $z$ -space, has been in use for a long time  
 177 (Bryan, 1962; Hall & Bryden, 1982; McDonagh et al., 2010; Piecuch et al., 2017). In this  
 178 method the heat transport by the overturning,  $\text{OHT}_{ot}^{(z)}(t)$ , is calculated by multiplying  
 179 the zonally-integrated velocity by the zonal-mean temperature, where all the zonal in-  
 180 tegrals are taken at constant depth, and then integrating in the vertical, so

$$\text{OHT}_{ot}^{(z)}(t) = \int_{-H}^0 \left( \int_{x_w}^{x_e} v(x, z, t) dx \right) \left( \frac{\int_{x_w}^{x_e} \theta(x, z, t) dx}{\int_{x_w}^{x_e} dx} \right) dz, \quad (4)$$

181 as illustrated in the top panel to figure 1. In this method, the heat transport by the gyre  
 182 is the total volume-conserving heat transport minus the heat transport by the overturn-  
 183 ing,

$$\text{OHT}_{gyre}^{(z)}(t) = \text{OHT}_{vc}(t) - \text{OHT}_{ot}^{(z)}(t), \quad (5)$$

184 where  $\text{OHT}_{ot}^{(z)}(t)$  is the heat transport attributed to the AMOC by the zonal-mean method  
 185 in  $z$ -space and  $\text{OHT}_{gyre}^{(z)}(t)$  is the heat transport attributed to the gyre by the zonal-mean  
 186 method in  $z$ -space.

187 The second method we investigate is similar to the first method, but zonal inte-  
 188 grals are taken in density coordinates instead of depth coordinates. Thickness-weighting  
 189 is necessary to preserve volume conservation (see e.g. Young (2012)), so

$$\begin{aligned} \text{OHT}_{ot}^{(\rho)}(t) &= \int_{\rho_{min}}^{\rho_{max}} \left( \int_{x_w}^{x_e} v(x, \rho, t) \zeta_{\bar{\rho}}(x, \rho, t) dx \right) \left( \frac{\int_{x_w}^{x_e} \theta(x, \rho, t) \zeta_{\bar{\rho}}(x, \rho, t) dx}{\int_{x_w}^{x_e} \zeta_{\bar{\rho}}(x, \rho, t) dx} \right) d\rho, \quad (6) \\ &\approx \sum_{\rho} \left( \int_{x_w}^{x_e} v(x, \rho, t) \delta z(x, \rho, t) dx \right) \left( \frac{\int_{x_w}^{x_e} \theta(x, \rho, t) \delta z(x, \rho, t) dx}{\int_{x_w}^{x_e} \delta z(x, \rho, t) dx} \right), \quad (7) \end{aligned}$$

190 where  $\zeta$  is the depth of a density surface and  $\zeta_{\bar{\rho}}$  is the derivative of  $\zeta$  with respect to den-  
 191 sity. When this calculation is discretized, a finite layer thickness  $\delta z$  is used to describe  
 192 the vertical distance between two isopycnals, and we sum over all densities. This method  
 193 is illustrated in the second panel of figure 1. As in the first method, the heat transport  
 194 by the gyre is the total volume-conserving heat transport minus the heat transport by

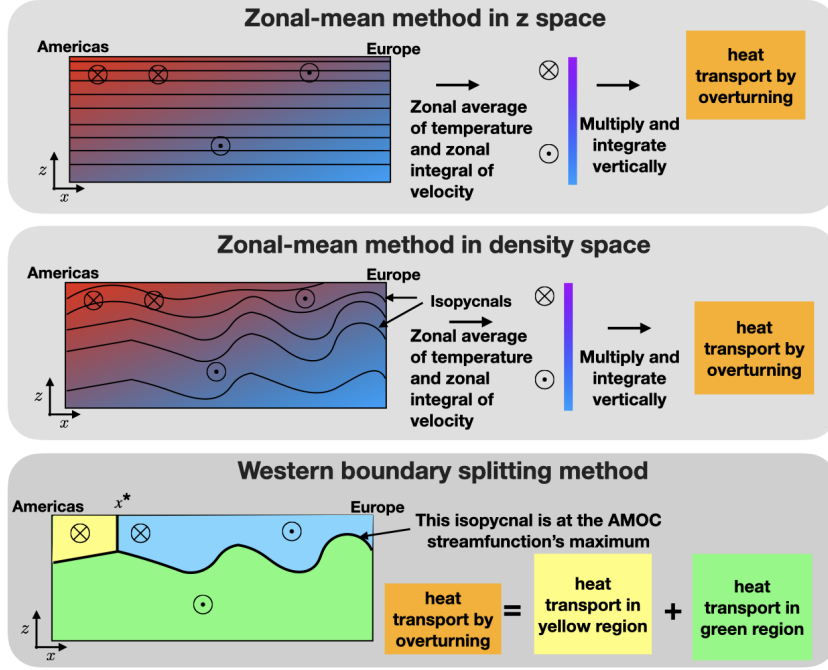


**Figure 1.** Schematic of three different methods for separating heat transport due to the overturning and heat transport due to the gyre.

the overturning,

$$\text{OHT}_{gyre}^{(\rho)}(t) = \text{OHT}_{vc}(t) - \text{OHT}_{ot}^{(\rho)}(t), \quad (8)$$

where  $\text{OHT}_{ot}^{(\rho)}(t)$  is the heat transport attributed to the AMOC by the zonal-mean method in density-space and  $\text{OHT}_{gyre}^{(\rho)}(t)$  is the heat transport attributed to the gyre by the zonal-mean method in density-space.

Our new method is motivated by the pathway of water in the northward limb of the AMOC, as illustrated by the pseudo-streamfunction (Jones & Cessi, 2018), which is plotted in figure 2,

$$\Phi = \int_{x_w}^x \int_{-H}^0 v \mathcal{H}(\rho - \rho_m) dz dx', \quad (9)$$

where  $\mathcal{H}$  is the Heaviside function and  $\rho_m$  is the isopycnal that passes through the maximum of the meridional overturning streamfunction (the yellow dashed-dotted line in figure 3).

As shown in figure 2, the AMOC's northward branch winds around the gyres, following the red contours northward. The blue contours in figure 2 represent the gyres. We expect that the strength of the gyres is independent of the strength of AMOC at long

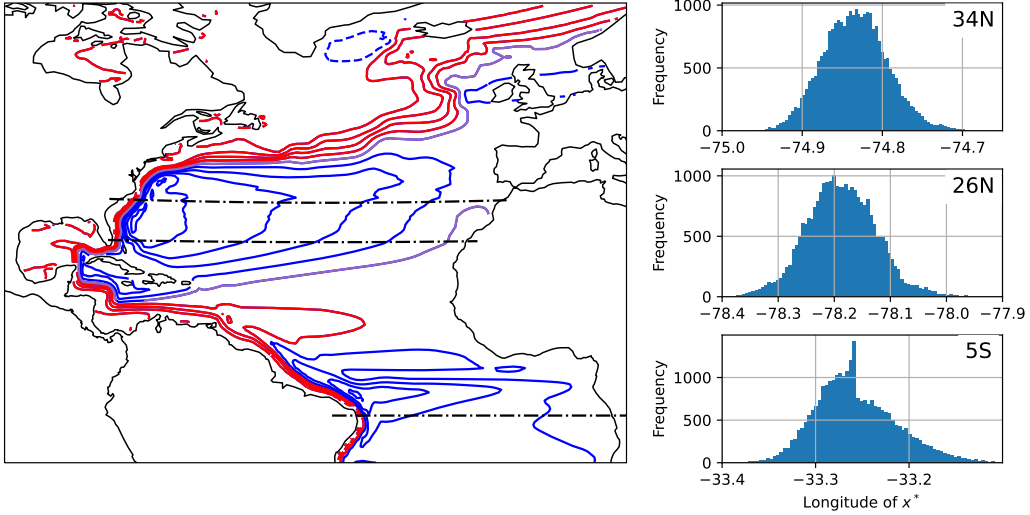


**Figure 2.** The red, blue and purple contours in the left panel show the pseudostreamfunction, the mean transport above  $\sigma_0 = 27.74$  (an isopycnal that passes through the maximum MOC streamfunction, as shown by the horizontal yellow line in figure 3) integrated from the western boundary eastward. The contour interval is 5 Sv. Red contours are contours that start in the south and end in the north, representing the AMOC. Blue contours are contours that cross each latitude twice, representing the gyres. The black dashed-dotted lines show the three latitudes used in this study. The right three panels are histograms of the location of  $x^*$ , the longitude that divides the AMOC transport and the gyre transport in the streamfunction splitting method (see the third panel of figure 1).

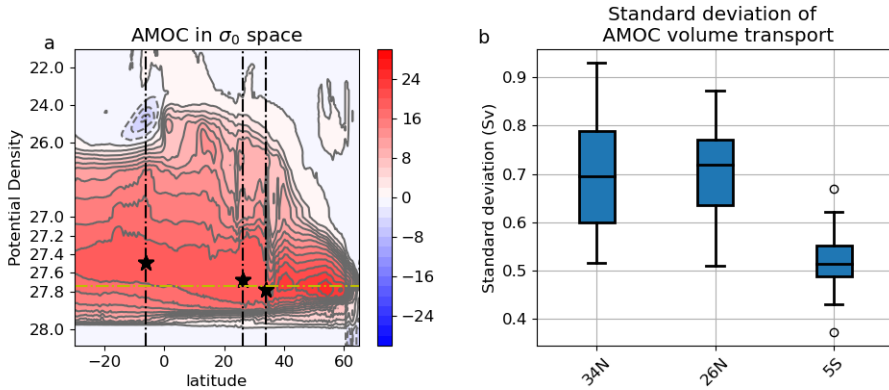


**Figure 3.** a) The Atlantic meridional overturning circulation in potential density space. b) The standard deviation of the AMOC volume transport at 34°N, 26°N and 5°S

208 timescales, and that the gyres are primarily driven by the wind, although recirculation  
 209 of northward AMOC transport may also be present.

210 Because the circulation is three-dimensional, the total transport above density sur-  
 211 face  $\rho_m$  contains a small divergent component, and  $\Phi$  is not a traditional streamfunc-  
 212 tion. A small number of open contours like the purple contour in figure 2 do not orig-  
 213 inate in the far south. These contours represent the movement of water that upwelled  
 214 across  $\rho_m$  within the domain.

215 In general, the red contours that represent the AMOC occupy the western bound-  
 216 ary only at latitudes with clockwise gyre circulation. In this paper, we focus on these  
 217 latitudes, because the AMOC pathway does not move around very much at these lat-  
 218 itudes. We plan to extend the method to other latitudes in future.

219 In our new method, which we call the streamfunction splitting method, a constant-  
 220 latitude section is divided into three regions. The first region is the deep region: this re-  
 221 gion is defined as the area below the dividing isopycnal, the green region in the bottom  
 222 panel of figure 1. This dividing isopycnal is chosen to be the isopycnal that passes through  
 223 the maximum of the meridional overturning streamfunction at that latitude (see stars  
 224 in figure 3a). The second region is the western-boundary region, the yellow region in the  
 225 bottom panel of figure 1, which is defined as the region above the dividing isopycnal and  
 226 west of the latitude  $x^*$ . Latitude  $x^*$  is chosen such that the volume transport through  
 227 the deep (green) region plus the volume transport through the western boundary (yel-  
 228 low) region sums to zero. The third region is the gyre region, the light blue region in the  
 229 bottom panel of figure 1, and this region is defined to be above the dividing isopycnal  
 230 and east of  $x^*$ . By definition, the volume transport through the gyre region is zero.

231 Here, we apply the streamfunction splitting method to the meridional velocity field  
 232 after performing a 24-month rolling time average in density space. Without this time-  
 233 average,  $x^*$  moves around a lot and sometimes is not defined. The dividing longitude  $x^*$   
 234 is shown in the right panels figure 2 at each latitude. Note that  $x^*$  is close to the west-  
 235 ern boundary in all cases, meaning that there is strong northward flow in the western  
 236 boundary current that is associated with AMOC.

237 Using a running mean that is applied after the heat transport is partitioned into  
 238 heat transport by the overturning and heat transport by the gyres, we further separate

239 the heat transport variability into variability on 2-10yr timescales and variability on 10+  
 240 year timescales. Ten years is chosen for ease of comparison with previous studies (e.g.  
 241 Larson et al. (2020)).

### 242 **3 Results**

#### 243 **3.1 AMOC variability in the CESM large ensemble**

244 AMOC variability is one cause of inter-decadal heat transport variability. Figure  
 245 3a shows the mean MOC as a function of density in the CESM large ensemble: the depth  
 246 and mean strength of the MOC does not vary much between ensemble members. The  
 247 mean AMOC volume transport is about 20 Sv.

248 Figure 3a shows the standard deviation of the smoothed AMOC volume transport  
 249 at three different latitudes. The latitude  $34^{\circ}\text{N}$  is chosen because it is the most northerly  
 250 latitude before the Gulf Stream separates in observations. In CESM1, the Gulf Stream  
 251 separation latitude is further north than Cape Hatteras, but we have chosen to use  $34^{\circ}\text{N}$   
 252 because this is the most northerly latitude where the western boundary current compares  
 253 well with observations. The latitude  $26^{\circ}\text{N}$  is chosen because it is the location of the RAPID  
 254 array.  $34^{\circ}\text{N}$  and  $26^{\circ}\text{N}$  are relatively close together, and we expect the results at these  
 255 latitudes to be relatively similar.  $5^{\circ}\text{S}$  was chosen to examine AMOC transport variabil-  
 256 ity near to the equator. AMOC variability is generally larger at  $34^{\circ}\text{N}$  and  $26^{\circ}\text{N}$  than at  
 257  $5^{\circ}\text{S}$ , as shown in figure 3b, so we expect that AMOC-driven heat transport variability  
 258 will be larger at  $34^{\circ}\text{N}$  and  $26^{\circ}\text{N}$  than at  $5^{\circ}\text{S}$ .

#### 259 **3.2 Heat transport variability in the CESM large ensemble**

260 Figure 4a-c shows the timeseries of heat and AMOC transport at the three cho-  
 261 sen latitudes for the third ensemble member, which is chosen as a representative ensem-  
 262 ble member. Heat transport is strongly correlated with AMOC at all three latitudes and  
 263 for both timescales of variability shown here (orange and blue lines in 4a-c).

264 Figure 4d-e shows the correlation between AMOC transport and heat transport  
 265 at the three chosen latitudes for all ensemble members, plotted as a function of the stan-  
 266 dard deviation of AMOC strength. Values further to the right have more AMOC vari-  
 267 ability and values further up have larger correlations between AMOC and AMOC heat  
 268 transport. Both AMOC variability and its correlation with heat transport are stronger

269 at 34°N and 26°N than at 5°S on 2-10yr timescales (figure 4d) and on 10+yr timescales  
 270 (figure 4e).

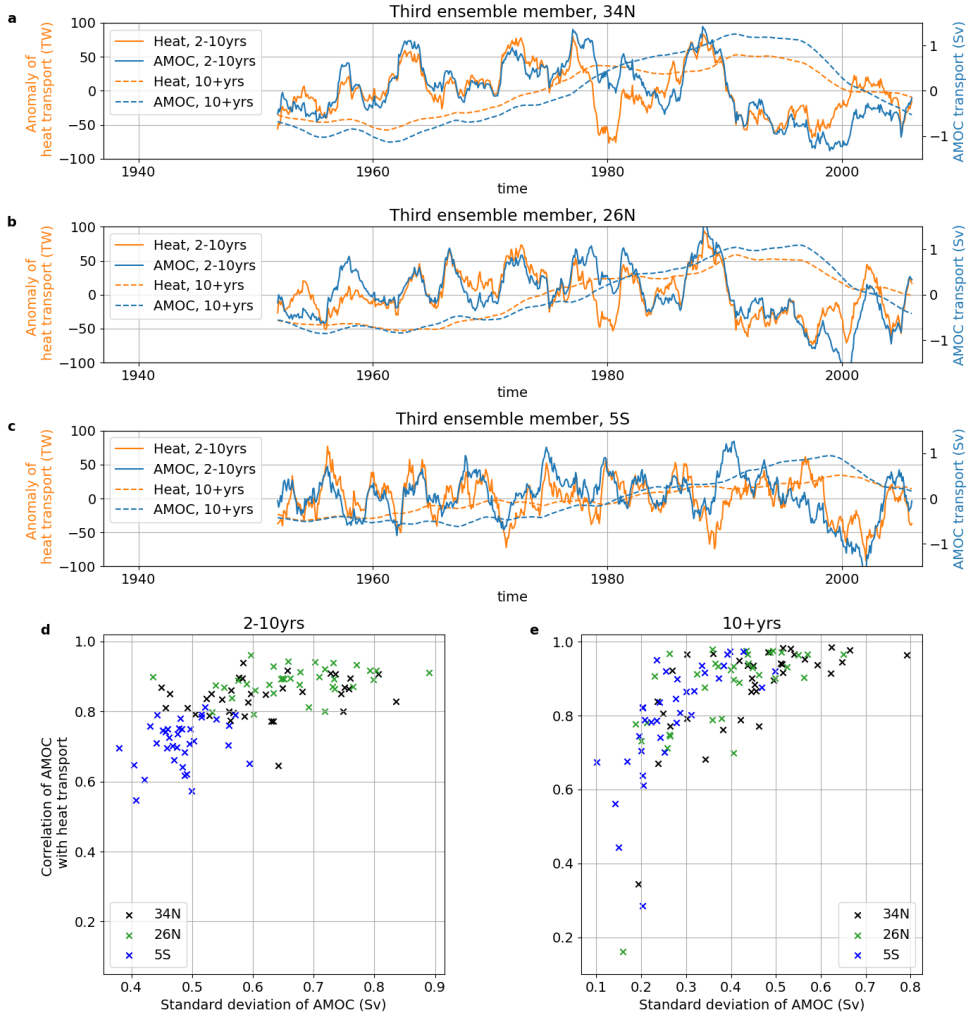


**Figure 4.** Timeseries of AMOC transport (blue) and heat transport (orange) for the third ensemble member, filtered to pick out variability on 2-10yr timescales (solid lines) and 10+yr timescales (dashed lines) at a) 34°N, b) 26°N and c) 5°S. The correlation between the smoothed heat transport and the smoothed AMOC transport at 34°N, 26°N and 5°S, plotted as a function of the standard deviation of the AMOC, filtered to pick out variability on d) 2-10yr timescales and e) 10+yr timescales (dashed lines). Each cross represents one ensemble member.

271 Most ensemble members show stronger correlations between AMOC and heat trans-  
 272 port at 10+yr timescales than at 2-10yr timescales, consistent with the idea that wind-  
 273 driven gyre variability is averaged out on timescales larger than 10 years. At all latitudes,

274 there are stronger correlations between AMOC and OHT in ensemble members with higher  
 275 AMOC variability.

276 Given the strong correlation between AMOC and OHT, it should be straightfor-  
 277 ward to decompose the component of OHT variability driven by AMOC variability. The  
 278 remainder of this work aims to elucidate the controls on heat transport at these differ-  
 279 ent latitudes and to compare methods for separating northward heat transport by the  
 280 gyres from northward heat transport by the overturning circulation.

### 281 **3.3 Heat transport by the gyres vs. heat transport by the overturning**

282 The mean meridional velocity in the first ensemble member at 34°N is shown in  
 283 figure 5a. The black contour indicates the mean depth of the isopycnal  $\rho_m$  and the hatched  
 284 region is the gyre region used in the streamfunction splitting method. The grey contour  
 285 indicates the topography. At this latitude, most of the northward flow in the western bound-  
 286 ary current is part of the AMOC. Southward flow at depth is not confined to the west-  
 287 ern boundary, but also occurs on the eastern flank of the mid-Atlantic ridge. The gyre  
 288 region contains both northward and southward velocities.

289 The heat transport at 34°N was separated into the heat transport by the net vol-  
 290 ume transport, the heat transport by the gyres and the heat transport by the overturn-  
 291 ing circulation using the three methods described in section 2.1. The results are plot-  
 292 ted in panels c and d of figure 5. All three methods give significantly different results.

293 In most ensemble members, the zonal-mean method in  $z$ -space attributes about 90%  
 294 of the heat transport to the overturning at 2-10 yr timescales (green box in figure 5c)  
 295 and at multidecadal timescales (green box in figure 5d), meaning that the gyre is respon-  
 296 sible for about 10% of the heat transport variability. Conceptual arguments suggest that  
 297 the zonal-mean method in  $z$ -space is likely to underestimate the heat transport variabil-  
 298 ity due to AMOC. In the zonal-mean method, the zonal mean temperature is multiplied  
 299 by the zonal integral of the velocity, even though most of the transport of the AMOC  
 300 follows the western boundary, where temperatures are much higher. At 34°N, the zonal  
 301 and depth mean temperature in the top 100m is about 20.2°C. West of 74.5°W (in the  
 302 western boundary where the AMOC is flowing northward), the zonal and depth mean  
 303 temperature in the top 100m is about 23.3°C. Hence we expect that the zonal-mean method  
 304 in  $z$ -space underestimates the heat transport variability due to AMOC at 34°N.

305 The zonal-mean method in density space attributes only about 45% of the heat trans-  
 306 port to the overturning on 2-10yr timescales and about 55% of the heat transport to the  
 307 overturning on 10+yr timescales. This is much lower than the other two methods, again  
 308 because AMOC variability mostly occurs on the western boundary at this latitude. Isopyc-  
 309 nals tilt upwards at the western boundary, and generally the water is warmer here. The  
 310 zonal average temperature in density space is much lower than the temperature on the  
 311 western boundary. As a result, the zonal-mean method in density space underestimates  
 312 the heat transport by the overturning even more than the zonal-mean method in  $z$ -space.

313 Our new method, which we call the western boundary splitting method, is not vul-  
 314 nerable to this problem. It attributes about 94% of the heat transport to the overturn-  
 315 ing in all ensemble members on 2-10yr timescales and about 120% of the heat transport  
 316 to the overturning on 10+yr timescales. More heat transport is attributed to AMOC than  
 317 one might expect based on the correlation between AMOC transport and the total heat  
 318 transport. The extra variability is compensated by heat transport attributed to the gyre,  
 319 which is anti-correlated with AMOC transport at 10+yr timescales.

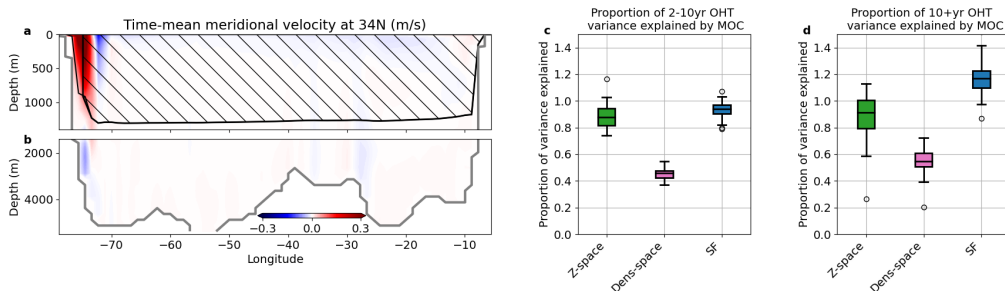


**Figure 5.** a and b show the time-mean meridional velocity at  $34^{\circ}\text{N}$  for the first ensemble member. The black contour shows the time-mean depth of the isopycnal that passes through the AMOC stream function's maximum. The hatched area is the area associated with the gyre in the streamfunction splitting method. The black vertical line shows the median location of  $x^*$ . c) A box and whisker plot of the heat transport on 2-10 yr timescales explained by each method, where the green box represents the proportion of variance explained by AMOC for the zonal-mean method in  $z$  space, the pink box represents the proportion of variance explained by AMOC for the zonal-mean method in density space, and the blue box represents the variance explained by AMOC for the streamfunction-splitting method. d) A box and whisker plot of the heat transport on 10+ yr timescales explained by each method (colors as in c).

320 At 26°N, both the zonal-mean method in  $z$ -space and the western boundary split-  
 321 ting method attribute about 100% of the heat transport variability to the AMOC on 2-  
 322 10yr timescales, while the zonal-mean method in density space attributes only 50% of  
 323 the heat transport to the AMOC (figure 6c). For the reasons described above, the zonal-  
 324 mean method in density space under-estimates the part of the heat transport that is per-  
 325 formed by the AMOC. On 10+yr timescales, the zonal-mean method in  $z$ -space again  
 326 attributes about 100% of the variability to AMOC, whereas the streamfunction split-  
 327 ting method attributes 120% of variability to AMOC, with some compensation between  
 328 the AMOC and gyres. Unlike other methods, it is clear what this compensation means  
 329 in the streamfunction splitting method. Times with high heat transport in the western  
 330 boundary are associated with times of low heat transport in the gyre region and vice versa.  
 331 This can easily be explained: when the AMOC transport is larger, more heat is trans-  
 332 ported northward and temperatures north of 26°N increase, reducing the difference in  
 333 temperature between northward and southward flowing water in the gyre region.

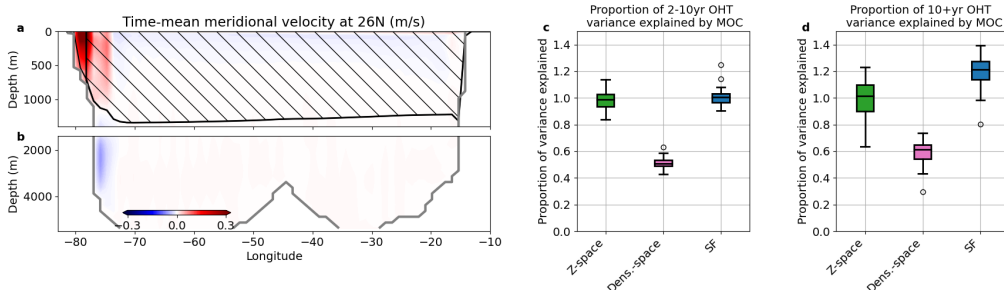


**Figure 6.** a and b show the time-mean meridional velocity at 26°N for the first ensemble member. The black contour shows the time-mean depth of the isopycnal that passes through the AMOC stream function’s maximum. The hatched area is the area associated with the gyre in the streamfunction splitting method. The black vertical line shows the median location of  $x^*$ . c) A box and whisker plot of the heat transport on 2-10 yr timescales explained by each method, where the green box represents the proportion of variance explained by AMOC for the zonal-mean method in  $z$  space, the pink box represents the proportion of variance explained by AMOC for the zonal-mean method in density space, and the blue box represents the variance explained by AMOC for the streamfunction-splitting method. d) A box and whisker plot of the heat transport on 10+ yr timescales explained by each method (colors as in c).

334 Because  $26^{\circ}\text{N}$  and  $34^{\circ}\text{N}$  are close together and both occur in the subtropical gyre,  
 335 we expect that heat transport by the overturning at  $26^{\circ}\text{N}$  and at  $34^{\circ}\text{N}$  are similar to each  
 336 other, particularly at long timescales. In figure 7, we plot the correlation between the  
 337 heat transport by the overturning at  $26^{\circ}\text{N}$  and at  $34^{\circ}\text{N}$  for the 2-10yr timescale and for  
 338 the 10+yr timescale. The zonal-mean method in density space and the streamfunction  
 339 splitting method both find strong correlations between ocean heat transport attributed  
 340 to overturning at  $26^{\circ}\text{N}$  and at  $34^{\circ}\text{N}$ , while the zonal-mean method in  $z$ -space generally  
 341 finds weaker correlations between the two latitudes. This is particularly obvious at 10+yr  
 342 timescales, for which the correlation between  $26^{\circ}\text{N}$  and at  $34^{\circ}\text{N}$  is close to one for the  
 343 streamfunction splitting method. This suggests that the zonal-mean method in  $z$ -space  
 344 is less robust than the other two methods, and may give different results even at sim-  
 345 ilar latitudes.

346 At  $5^{\circ}\text{S}$ , the zonal-mean method in  $z$ -space attributes about 85% of the heat trans-  
 347 port to AMOC on 2-10yr timescales (figure 8c). The zonal-mean method in density space  
 348 attributes less than 20% of the heat transport to AMOC, again suggesting that this method  
 349 severely underestimates the role of overturning in heat transport. The streamfunction  
 350 splitting method attributes about 55% of heat transport variability to AMOC. One rea-  
 351 son why the zonal-mean method in  $z$ -space and the streamfunction splitting method give  
 352 such different results is that the zonal-mean method in  $z$ -space counts the subtropical  
 353 cell in the overturning transport. The subtropical cell is primarily a vertical circulation  
 354 that comprises poleward flow very close to the surface and equatorward flow in the top  
 355 100m or so of the water column: because of the strong temperature contrast between these  
 356 two parts of the flow, the subtropical cell transports a lot of heat. The streamfunction  
 357 splitting method counts the most of the subtropical cell in the gyre transport, because  
 358 it takes place away from the western boundary.

359 At 10+yr timescales, the zonal-mean method in  $z$ -space and the streamfunction-  
 360 splitting method estimate that about 80% of heat transport variability is attributed to  
 361 the overturning (figure 8d). This is plausible, because the variability of the subtropical  
 362 cell generally has much shorter timescales. There is a wide variation between ensemble  
 363 members, possibly caused by low heat transport variability at this latitude on 10+yr timescales.  
 364 As above, the zonal-mean method in density space severely underestimates the role of  
 365 overturning in heat transport

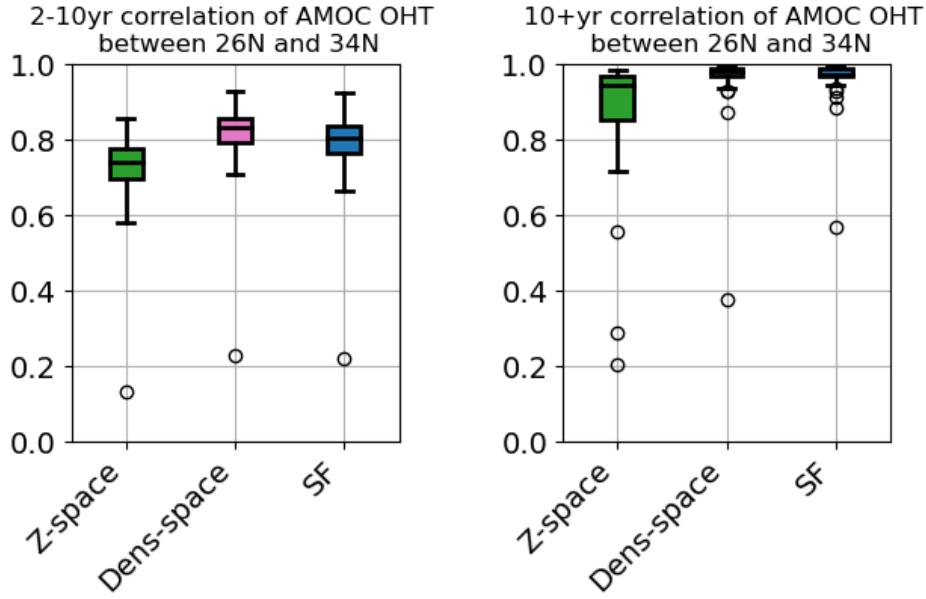


**Figure 7.** The left panel shows box and whisker plots of the correlation between the ocean heat transport attributed to AMOC at  $26^{\circ}\text{N}$  and at  $34^{\circ}\text{N}$  for each ensemble member, filtered to select 2-10yr timescales. The right panel shows the same, but filtered to select 10+ yr timescales. The green box represents the correlation between OHT explained by AMOC between  $26^{\circ}\text{N}$  and  $34^{\circ}\text{N}$  for the zonal-mean method in z space, the pink box represents the proportion of variance explained by AMOC for the zonal-mean method in density space, and the blue box represents the variance explained by AMOC for the streamfunction-splitting method

#### 366 4 Conclusions

367 In this paper, we present three methods for partitioning the AMOC heat transport  
 368 and the gyre heat transport in the Atlantic basin. The first two methods have been used  
 369 in the past: both methods estimate the heat transport by the AMOC using the prod-  
 370 uct of the zonal-mean temperature and the zonally-integrated volume transport. The  
 371 first method takes the zonal mean and zonal integral in depth space: we call this method  
 372 the zonal-mean method in  $z$ -space. The second method takes the zonal mean and zonal  
 373 integral in density space: we call this method the zonal-mean method in density-space.  
 374 The third method is a new method which uses physical information about the pathway

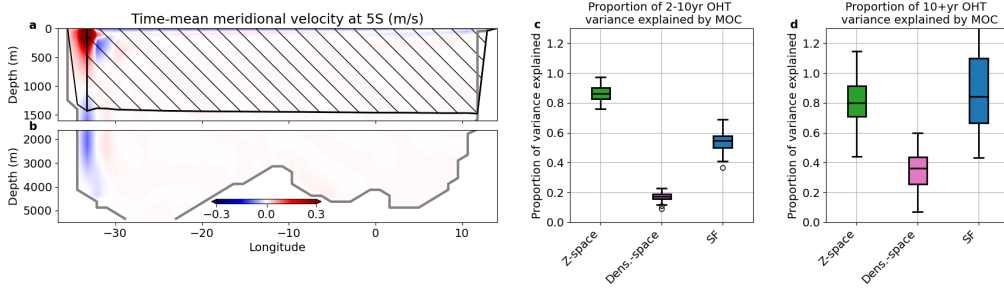


**Figure 8.** Total heat transport, heat transport by the net volume transport, heat transport by the overturning and heat transport by the gyres at  $5^{\circ}\text{S}$ , for a,c,e the third ensemble member and b,d,f the sixth ensemble member using a, b, the zonal-mean method in  $z$ -space, c, d, the zonal-mean method in density space, and e, f the western boundary splitting method. g) A box and whisker plot of the heat transport explained by each method.

375 of the AMOC to partition the two components of the heat transport. We call this method  
 376 the streamfunction splitting method.

377 We compare the methods at three different latitudes:  $34^{\circ}\text{N}$ ,  $26^{\circ}\text{N}$  and  $5^{\circ}\text{S}$ . At all  
 378 of these latitudes, the zonal-mean method in depth space and the zonal-mean method  
 379 in density space perform very differently from each other. The zonal-mean method in  
 380 in density space always attributes greater than 40% of heat transport to the gyre, and at  
 381  $5^{\circ}\text{S}$ , it attributes more than 70% of heat transport to the gyre. Given the strong cor-  
 382 relation between AMOC and heat transport at all three latitudes, it seems unlikely that  
 383 the gyre plays such a large role in heat transport. We find that the zonal-mean method  
 384 in density space is ineffective for partitioning the heat transport by the overturning and  
 385 the heat transport by the gyres.

386 The zonal-mean method in depth space and our new method sometimes give sim-  
 387 ilar results, but at  $34^{\circ}\text{N}$  and at  $26^{\circ}\text{N}$  the zonal-mean method in  $z$ -space indicates that  
 388 80% to 100% of multidecadal variability is explained by AMOC, with little compensa-  
 389 tion between the heat transport by the AMOC and the heat transport by the gyres. Like  
 390 the zonal-mean method in density space, the zonal-mean method in  $z$ -space underesti-  
 391 mates the heat transport variability due to AMOC because the zonally-integrated tem-  
 392 perature is smaller than the temperature of the northward-flowing AMOC transport. Our  
 393 new streamfunction-splitting method uses recent understanding of AMOC as a circula-  
 394 tion in density space, but also applies a new insight: that AMOC follows the western bound-

395 ary when it flows past clockwise gyre circulations. Hence, our new method does not use  
396 a zonal average and is not vulnerable to underestimating AMOC heat transport due to  
397 averaging over the whole width of the basin.

398 The new method presented here indicates that in CESM, heat transport by the AMOC  
399 explains about 120% of the multidecadal heat transport variability at 26°N and 34°N  
400 (with 20% compensated by southward heat transport in the gyre), and 80% of the heat  
401 transport variability at 5°S. Unlike the zonal-mean method in  $z$ -space, on long timescales  
402 our new method gives very similar results at latitudes that are close to each other. While  
403 our new method is difficult to apply directly to observations, it can be applied to any  
404 model and a long timeseries is not necessary.

405 At 5°S, the subtropical cell contributes to the vertical part of the meridional heat  
406 transport, but may or may not be considered part of the AMOC. Both the zonal-mean  
407 method in  $z$ -space and the streamfunction-splitting method are somewhat informative  
408 at this latitude: their differences highlight that much of the subtropical cell is found out-  
409 side the western boundary, and that the subtropical cell is a significant cause of heat trans-  
410 port variability on 2-10yr timescales. Future studies using Lagrangian particles could help  
411 elucidate how the subtropical cell and the upper cell of the AMOC are connected.

## 412 **5 Open Research**

413 The code repository for this paper is at [https://github.com/cspencerjones/amoc](https://github.com/cspencerjones/amoc_heat_code)  
414 [\\_heat\\_code](#). The data used in this research is the CESM1 Large Ensemble, which is hosted  
415 on Amazon Web Services (de La Beaujardiere et al., 2019). This work would not have  
416 been possible without the tools provided by and maintained by the Pangeo community  
417 (<https://pangeo.io/>).

## 418 **Acknowledgments**

419 Thanks to Navid Constantinou for several useful discussions about this work. CSJ's work  
420 on this project was supported by NSF award number OCE-2219852.

## 421 **References**

422 Bhagtani, D., Hogg, A. M., Holmes, R. M., & Constantinou, N. C. (2023). Surface  
423 heating steers planetary-scale ocean circulation. *Journal of Physical Oceanog-*

- 424            *raphy*.
- 425    Boccaletti, G., Ferrari, R., Adcroft, A., Ferreira, D., & Marshall, J. (2005). The ver-  
426            tical structure of ocean heat transport. *Geophysical Research Letters*, *32*(10).
- 427    Borchert, L. F., Müller, W. A., & Baehr, J. (2018). Atlantic ocean heat transport  
428            influences interannual-to-decadal surface temperature predictability in the  
429            north atlantic region. *Journal of Climate*, *31*(17), 6763–6782.
- 430    Bryan, K. (1962). Measurements of meridional heat transport by ocean currents.  
431            *Journal of Geophysical Research*, *67*(9), 3403–3414.
- 432    Buckley, M. W., & Marshall, J. (2016). Observations, inferences, and mechanisms  
433            of the Atlantic Meridional Overturning Circulation: A review. *Reviews of Geo-*  
434            *physics*, *54*(1), 5–63.
- 435    Cessi, P. (2018). The effect of Northern Hemisphere winds on the meridional over-  
436            turning circulation and stratification. *Journal of Physical Oceanography*,  
437            *48*(10), 2495–2506.
- 438    de La Beaujardiere, J., Banihirwe, A., Shih, C., Paul, K., & Hamman, J. (2019).  
439            NCAR CESM LENS cloud-optimized subset. *UCAR/NCAR Computational*  
440            *and Informations Systems Lab*. doi: 10.26024/wt24-5j82
- 441    Eden, C., & Willebrand, J. (2001). Mechanism of interannual to decadal variability  
442            of the North Atlantic circulation. *Journal of Climate*, *14*(10), 2266–2280.
- 443    Ferrari, R., & Ferreira, D. (2011). What processes drive the ocean heat transport?  
444            *Ocean Modelling*, *38*(3-4), 171–186.
- 445    Folland, C. K., Palmer, T. N., & Parker, D. E. (1986). Sahel rainfall and worldwide  
446            sea temperatures, 1901–85. *Nature*, *320*(6063), 602–607.
- 447    Foukal, N. P., & Chafik, L. (2022). The AMOC needs a universally-accepted defini-  
448            tion. *Authorea Preprints*.
- 449    Goldenberg, S. B., Landsea, C. W., Mestas-Nuñez, A. M., & Gray, W. M. (2001).  
450            The recent increase in Atlantic hurricane activity: Causes and implications.  
451            *Science*, *293*(5529), 474–479.
- 452    Gray, A. R., & Riser, S. C. (2014). A global analysis of Sverdrup balance using  
453            absolute geostrophic velocities from Argo. *Journal of Physical Oceanography*,  
454            *44*(4), 1213–1229.
- 455    Hall, M. M., & Bryden, H. L. (1982). Direct estimates and mechanisms of ocean  
456            heat transport. *Deep Sea Research Part A. Oceanographic Research Papers*,

457 29(3), 339–359.

458 Jackson, L., Kahana, R., Graham, T., Ringer, M., Woollings, T., Mecking, J., &  
459 Wood, R. (2015). Global and European climate impacts of a slowdown of the  
460 AMOC in a high resolution GCM. *Climate dynamics*, 45, 3299–3316.

461 Jones, C., & Cessi, P. (2018). Components of upper-ocean salt transport by the  
462 gyres and the meridional overturning circulation. *Journal of Physical Oceanog-*  
463 *raphy*, 48(10), 2445–2456.

464 Kang, S. M., Frierson, D. M., & Held, I. M. (2009). The tropical response to ex-  
465 tratropical thermal forcing in an idealized GCM: The importance of radiative  
466 feedbacks and convective parameterization. *Journal of the atmospheric sci-*  
467 *ences*, 66(9), 2812–2827.

468 Kay, J. E., Deser, C., Phillips, A., Mai, A., Hannay, C., Strand, G., . . . others  
469 (2015). The Community Earth System Model (CESM) large ensemble project:  
470 A community resource for studying climate change in the presence of internal  
471 climate variability. *Bulletin of the American Meteorological Society*, 96(8),  
472 1333–1349.

473 Klotzbach, P., Gray, W., & Fogarty, C. (2015). Active Atlantic hurricane era at its  
474 end? *Nature Geoscience*, 8(10), 737–738.

475 Larson, S. M., Buckley, M. W., & Clement, A. C. (2020). Extracting the buoyancy-  
476 driven Atlantic meridional overturning circulation. *Journal of Climate*, 33(11),  
477 4697–4714.

478 Marshall, J., Donohoe, A., Ferreira, D., & McGee, D. (2014). The ocean’s role in  
479 setting the mean position of the Inter-Tropical Convergence Zone. *Climate Dy-*  
480 *namics*, 42, 1967–1979.

481 Martin, E. R., & Thorncroft, C. D. (2014). The impact of the AMO on the West  
482 African monsoon annual cycle. *Quarterly Journal of the Royal Meteorological*  
483 *Society*, 140(678), 31–46.

484 McDonagh, E. L., McLeod, P., King, B. A., Bryden, H. L., & Valdés, S. T. (2010).  
485 Circulation, heat, and freshwater transport at 36 N in the Atlantic. *Journal of*  
486 *physical oceanography*, 40(12), 2661–2678.

487 Oldenburg, D., Wills, R. C., Armour, K. C., Thompson, L., & Jackson, L. C. (2021).  
488 Mechanisms of low-frequency variability in North Atlantic Ocean heat trans-  
489 port and AMOC. *Journal of Climate*, 34(12), 4733–4755.

- 490 Pickart, R. S., & Spall, M. A. (2007). Impact of Labrador Sea convection on  
491 the North Atlantic meridional overturning circulation. *Journal of Physical*  
492 *Oceanography*, *37*(9), 2207–2227.
- 493 Piecuch, C. G., Ponte, R. M., Little, C. M., Buckley, M. W., & Fukumori, I. (2017).  
494 Mechanisms underlying recent decadal changes in subpolar North Atlantic  
495 Ocean heat content. *Journal of Geophysical Research: Oceans*, *122*(9), 7181–  
496 7197.
- 497 Roemmich, D., & Wunsch, C. (1985). Two transatlantic sections: Meridional circula-  
498 tion and heat flux in the subtropical North Atlantic Ocean. *Deep Sea Research*  
499 *Part A. Oceanographic Research Papers*, *32*(6), 619–664.
- 500 Rypina, I. I., Pratt, L. J., & Lozier, M. S. (2011). Near-surface transport pathways  
501 in the North Atlantic Ocean: Looking for throughput from the subtropical to  
502 the subpolar gyre. *Journal of Physical Oceanography*, *41*(5), 911–925.
- 503 Stommel, H. (1957). A survey of ocean current theory. *Deep Sea Research (1953)*, *4*,  
504 149–184.
- 505 Talley, L. D. (1999). Some aspects of ocean heat transport by the shallow, inter-  
506 mediate and deep overturning circulations. *Geophysical Monograph-American*  
507 *Geophysical Union*, *112*, 1–22.
- 508 Trenberth, K. E., & Fasullo, J. T. (2017). Atlantic meridional heat transports com-  
509 puted from balancing earth’s energy locally. *Geophysical Research Letters*,  
510 *44*(4), 1919–1927.
- 511 Warren, B. A. (1999). Approximating the energy transport across oceanic sections.  
512 *Journal of Geophysical Research: Oceans*, *104*(C4), 7915–7919.
- 513 Yan, X., Zhang, R., & Knutson, T. R. (2018). Underestimated AMOC variability  
514 and implications for AMV and predictability in CMIP models. *Geophysical Re-*  
515 *search Letters*, *45*(9), 4319–4328.
- 516 Yang, J. (2015). Local and remote wind stress forcing of the seasonal variability of  
517 the Atlantic Meridional Overturning Circulation (AMOC) transport at 26.5 N.  
518 *Journal of Geophysical Research: Oceans*, *120*(4), 2488–2503.
- 519 Yeager, S. G., Karspeck, A. R., & Danabasoglu, G. (2015). Predicted slowdown in  
520 the rate of Atlantic sea ice loss. *Geophysical Research Letters*, *42*(24), 10–704.
- 521 Young, W. R. (2012). An exact thickness-weighted average formulation of the  
522 Boussinesq equations. *Journal of Physical Oceanography*, *42*(5), 692–707.

- 523 Zhang, R., Sutton, R., Danabasoglu, G., Kwon, Y.-O., Marsh, R., Yeager, S. G., ...  
524 Little, C. M. (2019). A review of the role of the Atlantic meridional over-  
525 turning circulation in Atlantic multidecadal variability and associated climate  
526 impacts. *Reviews of Geophysics*, 57(2), 316–375.
- 527 Zhang, R., & Thomas, M. (2021). Horizontal circulation across density surfaces  
528 contributes substantially to the long-term mean northern Atlantic Meridional  
529 Overturning Circulation. *Communications Earth & Environment*, 2(1), 112.

1 **A new diagnostic for AMOC heat transport applied to**  
2 **the CESM large ensemble**

3 **C Spencer Jones<sup>1</sup>, Scout Jiang<sup>2</sup> and Ryan P. Abernathey<sup>2</sup>**

4 <sup>1</sup>Texas A&M University, College Station, TX

5 <sup>2</sup>Columbia University, New York, NY

6 **Key Points:**

- 7 • We introduce a new diagnostic for AMOC heat transport that partitions the flow  
8 into mass-conserving gyre and overturning components
- 9 • The new method is compared with the standard method that relies on zonally av-  
10 eraging the temperature and velocity fields
- 11 • The new method provides a clearer way of separating heat transport by the gyres  
12 and by the overturning

---

Corresponding author: C. Spencer Jones, [spencerjones@tamu.edu](mailto:spencerjones@tamu.edu)

**Abstract**

Atlantic time-mean heat transport is northward at all latitudes and exhibits strong multidecadal variability between about 30°N and 55°N. Atlantic heat transport variability influences many aspects of the climate system, including regional surface temperatures, subpolar heat content, Arctic sea-ice concentration and tropical precipitation patterns. Atlantic heat transport and heat transport variability are commonly partitioned into two components: the heat transport by the AMOC and the heat transport by the gyres. In this paper we compare three different methods for performing this partition, and we apply these methods to the CESM1 Large Ensemble at 34°N, 26°N and 5°S. We discuss the strengths and weaknesses of each method. One of these methods is a new physically-motivated method based on the pathway of the northward-flowing part of AMOC. This paper presents a preliminary version of our method. This preliminary version works only when the AMOC follows the western boundary of the basin. In this context, the new method provides a sensible estimate of heat transport by the overturning and by the gyre, and it is easier to interpret than other methods. According to our new diagnostic, at 34°N and at 26°N AMOC explains 120% of the multidecadal variability (20% is compensated by the gyre), and at 5°S AMOC explains 90% of multidecadal variability.

**Plain Language Summary**

Scientists often want to quantify how much heat is transported by the Atlantic Meridional Overturning Circulation (sometimes called the “Conveyor Belt” circulation) and how much heat is transported by the ocean’s gyres. This paper compares some different methods for estimating the heat transport by the overturning circulation and by the gyres, including a new method that has not been used before. While previous methods are easier to apply to observations, the new method gives results that are easier to understand.

**1 Introduction**

The Atlantic Meridional Overturning Circulation (AMOC) comprises northward flow of warmer water near the surface, deep water formation in the North Atlantic, and southward flow of cooler water at depth. The AMOC transports heat northward throughout the Atlantic basin, warming the Northern Hemisphere (Jackson et al., 2015; Buckley & Marshall, 2016) and performing 20% of the total planetary poleward heat trans-

44 port at 26.5°N (Trenberth & Fasullo, 2017). The AMOC’s cross-equatorial heat trans-  
45 port shifts the intertropical convergence zone (ITCZ) northward, affecting precipitation  
46 patterns close to the equator (Kang et al., 2009; Marshall et al., 2014).

47 Variations in northward Atlantic heat transport are thought to be a key driver of  
48 Atlantic Multidecadal Variability (Oldenburg et al., 2021), which affects variability in mul-  
49 tiple parts of the climate system (Zhang et al., 2019), including tropical precipitation  
50 (Folland et al., 1986; Martin & Thorncroft, 2014), Atlantic hurricane frequency (Goldenberg  
51 et al., 2001; Klotzbach et al., 2015), and North Atlantic sea ice variability (Yeager et al.,  
52 2015). Low frequency ocean variability is a source of predictability in the climate sys-  
53 tem, meaning that parts of the climate system that are driven by AMOC variability may  
54 be predictable using observations of the ocean (Borchert et al., 2018). AMOC low-frequency  
55 variability and Atlantic decadal predictability vary significantly between climate mod-  
56 els (Yan et al., 2018). To understand the cause of differences between models, it is help-  
57 ful to characterize how the AMOC and the gyres interact to influence northward ocean  
58 heat transport. In this paper, we use three different methods to estimate how much ocean  
59 heat transport is performed by AMOC.

60 Many studies have attempted to separate the heat transport by the overturning  
61 circulation from the heat transport by the gyres (e.g. Bryan (1962); Hall and Bryden  
62 (1982); McDonagh et al. (2010); Ferrari and Ferreira (2011); Piecuch et al. (2017)). Most  
63 studies suggest that AMOC is the primary driver of heat transport in the subtropical  
64 gyre region and that the gyre is a more important driver in the subpolar gyre region (Eden  
65 & Willebrand, 2001; Piecuch et al., 2017). Many of the studies that have partitioned the  
66 heat transport by the gyres and the heat transport by the overturning circulation have  
67 done so with the goal of identifying how much of the heat transport variability is driven  
68 by wind and how much is driven by buoyancy forcing. AMOC variability is often thought  
69 to be primarily driven by buoyancy forcing, and the gyres are thought to be primarily  
70 driven by wind forcing. But recent studies have shown that gyre strength is strongly in-  
71 fluenced by buoyancy forcing (Bhagtani et al., 2023), and that AMOC strength is strongly  
72 influenced by wind forcing (Yang, 2015; Cessi, 2018). The goal of this study is not to par-  
73 tition the heat transport caused by wind from the heat transport caused by buoyancy  
74 forcing, but to elucidate how the total AMOC transport influences heat transport at mul-  
75 tiple latitudes, and to clarify whether this heat transport takes place on the western bound-  
76 ary or in the interior of the basin.

77 Most previous studies define the heat transport by the overturning as the zonal in-  
78 tegral of the volume transport multiplied by the zonal mean temperature, integrated in  
79 the vertical. In all the studies that use this method, the integrals are taken in depth space.  
80 In the last twenty years or so, oceanographers have started to define the AMOC using  
81 a zonal-average in density space (Foukal & Chafik, 2022). Recent work by Zhang and  
82 Thomas (2021) has shown that flows on the same depth level in the subpolar gyre re-  
83 gion have different densities and form part of the AMOC. It is clear that the old depth-  
84 averaged way of looking at things can still be useful, but much progress has been made  
85 by looking at the AMOC in new ways.

86 In this work, we introduce a new method for partitioning the heat transport due  
87 to the overturning and the heat transport due to the gyres based on a more nuanced un-  
88 derstanding of the circulation patterns. Northward flow in the North Atlantic is dom-  
89 inated by the Gulf Stream. The Gulf Stream is significantly stronger than required to  
90 satisfy Sverdrup balance (Gray & Riser, 2014), which can partly be attributed to the pres-  
91 ence of an additional flow component: the northward component of the AMOC. AMOC  
92 transport primarily follows the western boundary at latitudes where the gyre is clock-  
93 wise (Stommel, 1957). Rypina et al. (2011) showed that drifters in the far west of the  
94 Gulf Stream are likely to reach the North Atlantic, whereas drifters further to the east  
95 are unlikely to cross northward into latitudes associated with the subpolar gyre. In this  
96 work we extend this idea, splitting the upper part of the ocean into AMOC transport,  
97 which follows the western boundary, and gyre transport, which occupies the interior.

98 Our method is conceptually similar to a method used by Roemmich and Wunsch  
99 (1985). Roemmich and Wunsch (1985) estimated the temperature transport in the deep  
100 ocean, the temperature transport in the western boundary current, and the temperature  
101 transport in the southward flowing part of the gyre from observations. Talley (1999) used  
102 a similar method. These authors took the mean temperature in the western boundary  
103 current and calculated the heat transport by the AMOC to be the volume transport of  
104 the AMOC multiplied the difference in temperature between the western boundary cur-  
105 rent and the deep ocean. They applied their method to sections at 24°N and found that  
106 90% of the mean northward heat transport is performed by the AMOC at this latitude,  
107 and they commented that the northward heat transport is dominated by the AMOC across  
108 multiple years of observations. Because our new method is applied to a model, we are  
109 able to more clearly define the regions associated with the AMOC and with the gyre.

110 In this work, we compare three methods for partitioning ocean heat transport into  
111 heat transport by the overturning and heat transport by the gyres. We use the CESM  
112 large ensemble as a testbed for these different methods, because the existence of long runs  
113 and many ensemble members allows us to examine variability at multiple timescales. The  
114 CESM large ensemble is described in section 2 and the three methods for partitioning  
115 heat transport by the overturning and heat transport by the gyres are described in sec-  
116 tion 2.1. Sections 3.1 and 3.2 describe the total AMOC and heat transport variability  
117 in the CESM large ensemble, and section 3.3 shows the results of different methods for  
118 partitioning the heat transport by the overturning and the heat transport by the gyres.  
119 Section 4 discusses the results and presents conclusions.

## 120 **2 Methods**

121 We explore these diagnostics in the context of ocean models, where the time vary-  
122 ing circulation and temperature fields are perfectly known. Our analysis uses a large en-  
123 semble of ocean simulation in order to sample broadly the modes of natural variability  
124 of the North Atlantic circulation. The CESM Large Ensemble is a group of simulations  
125 performed using a  $1^\circ$  nominal resolution fully-coupled version of the Community Earth  
126 System Model (CESM1) (Kay et al., 2015). Forty ensemble members were created for  
127 the period 1920-2100. Each ensemble member has the same radiative forcing scenario,  
128 but the initial atmospheric temperature is perturbed with a spatially random perturba-  
129 tion order  $10^{-14}$ K. As a result of internal variability, each ensemble member’s state fol-  
130 lows a unique trajectory with different regional temperature patterns and different AMOC  
131 variability.

132 We used the cloud-optimized dataset, which is stored on Amazon Web Services (AWS)  
133 thanks to the AWS Public Dataset Program (de La Beaujardiere et al., 2019). In this  
134 work we used the first 35 ensemble members for the period 1940-2005. 1940 is chosen  
135 because this allows time for the internal variability of the system to diverge, so that the  
136 ensemble members are different from each other throughout the chosen period. 2005 is  
137 a natural end date, because it marks the end of the historical runs for the CESM1 Large  
138 Ensemble. During the period 1940-2005 multidecadal variability dominates over long-  
139 term trends in AMOC and heat transport. Members of the CESM large ensemble are  
140 not meant to have exactly the same variability as the real world, but to represent the  
141 range of possible internal variability. Many of the ensemble members exhibit North At-

142 lantic subpolar gyre ocean heat content variability with similar magnitude to ECCOv4r3  
 143 (not shown).

## 144 **2.1 Separating heat transport by the gyre from heat transport by the** 145 **overturning circulation**

146 Heat transport by each gyre is primarily wind driven, and is likely to have short  
 147 time scales and spatial effects that are confined to that gyre. Heat transport by the over-  
 148 turning is both wind and buoyancy driven, and is more likely to impact temperatures  
 149 in the far North Atlantic. Hence, it is desirable to partition the heat transport across  
 150 a particular latitude into the heat transport by the overturning and the heat transport  
 151 by the gyres. All the methods described in this section are designed to be applied at a  
 152 fixed latitude. The notion of heat transport by the flow across a section is only well-defined  
 153 when the net mass transport (or volume transport, in a Boussinesq ocean model) of the  
 154 flow is zero (see e.g. Warren (1999); Boccaletti et al. (2005); Pickart and Spall (2007)).  
 155 In the Atlantic basin, there is a net southward volume transport of about 1 Sv, and the  
 156 heat transported by this net throughflow is dependent on our choice of reference tem-  
 157 perature. We still remove the net throughflow component of the heat transport. Because  
 158 the net throughflow is small, the results of this study are relatively insensitive to the choice  
 159 of reference temperature.

160 At each latitude, we remove the mean velocity from the total velocity to find the  
 161 volume conserving part of the velocity,

$$v_{vc}(x, z, t) = v(x, z, t) - \bar{v}(t), \quad (1)$$

162 where

$$\bar{v}(t) = \frac{\int_{-H}^0 \int_{x_w}^{x_e} v(x, z, t) dx dz}{\int_{-H}^0 \int_{x_w}^{x_e} dx dz}, \quad (2)$$

163 and  $x$  is distance in the longitudinal direction,  $z$  is distance in the vertical,  $v$  is the merid-  
 164 ional velocity,  $H$  is the ocean depth,  $x_w$  is the western boundary of the Atlantic and  $x_e$   
 165 is the eastern boundary of the Atlantic. Ideally, the residual velocity (including the eddy  
 166 transport) would be used in these calculations, but this data was not readily available,  
 167 so the effects of parameterized eddies are not included in  $v$ . We also remove the south-  
 168 ward heat transport that is associated with the mean velocity, so

$$\text{OHT}_{vc}(t) = \int_{-H}^0 \int_{x_w}^{x_e} v(x, z, t) \theta(x, z, t) dx dz - \int_{-H}^0 \int_{x_w}^{x_e} \theta(x, z, t) \bar{v}(t) dx dz, \quad (3)$$

169 where  $\theta$  is temperature.

170 The total volume conserving heat transport,  $\text{OHT}_{vc}$ , can be further decomposed  
 171 into the sum of heat transport by multiple sub-flows, provided that each sub-flow has  
 172 no net mass transport associated with it. There are infinitely many possible such decom-  
 173 positions. Once the net velocity and associated heat transport have been removed, we  
 174 apply and compare three methods for separating the heat transport by the overturning  
 175 and the heat transport by the gyres. These methods are illustrated in figure 1. The first  
 176 method, which we call the zonal-mean method in  $z$ -space, has been in use for a long time  
 177 (Bryan, 1962; Hall & Bryden, 1982; McDonagh et al., 2010; Piecuch et al., 2017). In this  
 178 method the heat transport by the overturning,  $\text{OHT}_{ot}^{(z)}(t)$ , is calculated by multiplying  
 179 the zonally-integrated velocity by the zonal-mean temperature, where all the zonal in-  
 180 tegrals are taken at constant depth, and then integrating in the vertical, so

$$\text{OHT}_{ot}^{(z)}(t) = \int_{-H}^0 \left( \int_{x_w}^{x_e} v(x, z, t) dx \right) \left( \frac{\int_{x_w}^{x_e} \theta(x, z, t) dx}{\int_{x_w}^{x_e} dx} \right) dz, \quad (4)$$

181 as illustrated in the top panel to figure 1. In this method, the heat transport by the gyre  
 182 is the total volume-conserving heat transport minus the heat transport by the overturn-  
 183 ing,

$$\text{OHT}_{gyre}^{(z)}(t) = \text{OHT}_{vc}(t) - \text{OHT}_{ot}^{(z)}(t), \quad (5)$$

184 where  $\text{OHT}_{ot}^{(z)}(t)$  is the heat transport attributed to the AMOC by the zonal-mean method  
 185 in  $z$ -space and  $\text{OHT}_{gyre}^{(z)}(t)$  is the heat transport attributed to the gyre by the zonal-mean  
 186 method in  $z$ -space.

187 The second method we investigate is similar to the first method, but zonal inte-  
 188 grals are taken in density coordinates instead of depth coordinates. Thickness-weighting  
 189 is necessary to preserve volume conservation (see e.g. Young (2012)), so

$$\begin{aligned} \text{OHT}_{ot}^{(\rho)}(t) &= \int_{\rho_{min}}^{\rho_{max}} \left( \int_{x_w}^{x_e} v(x, \rho, t) \zeta_{\bar{\rho}}(x, \rho, t) dx \right) \left( \frac{\int_{x_w}^{x_e} \theta(x, \rho, t) \zeta_{\bar{\rho}}(x, \rho, t) dx}{\int_{x_w}^{x_e} \zeta_{\bar{\rho}}(x, \rho, t) dx} \right) d\rho, \quad (6) \\ &\approx \sum_{\rho} \left( \int_{x_w}^{x_e} v(x, \rho, t) \delta z(x, \rho, t) dx \right) \left( \frac{\int_{x_w}^{x_e} \theta(x, \rho, t) \delta z(x, \rho, t) dx}{\int_{x_w}^{x_e} \delta z(x, \rho, t) dx} \right), \quad (7) \end{aligned}$$

190 where  $\zeta$  is the depth of a density surface and  $\zeta_{\bar{\rho}}$  is the derivative of  $\zeta$  with respect to den-  
 191 sity. When this calculation is discretized, a finite layer thickness  $\delta z$  is used to describe  
 192 the vertical distance between two isopycnals, and we sum over all densities. This method  
 193 is illustrated in the second panel of figure 1. As in the first method, the heat transport  
 194 by the gyre is the total volume-conserving heat transport minus the heat transport by

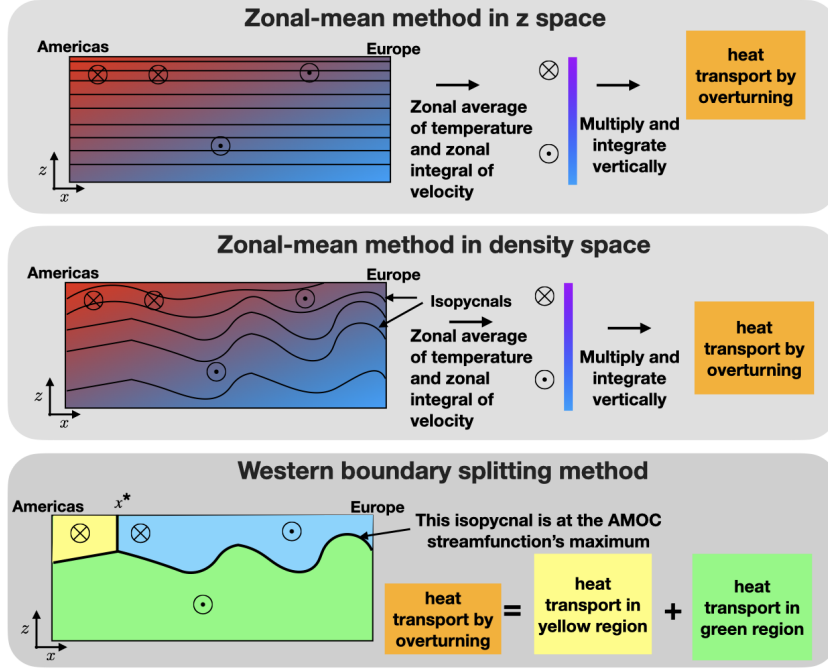


**Figure 1.** Schematic of three different methods for separating heat transport due to the overturning and heat transport due to the gyre.

the overturning,

$$\text{OHT}_{gyre}^{(\rho)}(t) = \text{OHT}_{vc}(t) - \text{OHT}_{ot}^{(\rho)}(t), \quad (8)$$

where  $\text{OHT}_{ot}^{(\rho)}(t)$  is the heat transport attributed to the AMOC by the zonal-mean method in density-space and  $\text{OHT}_{gyre}^{(\rho)}(t)$  is the heat transport attributed to the gyre by the zonal-mean method in density-space.

Our new method is motivated by the pathway of water in the northward limb of the AMOC, as illustrated by the pseudo-streamfunction (Jones & Cessi, 2018), which is plotted in figure 2,

$$\Phi = \int_{x_w}^x \int_{-H}^0 v \mathcal{H}(\rho - \rho_m) dz dx', \quad (9)$$

where  $\mathcal{H}$  is the Heaviside function and  $\rho_m$  is the isopycnal that passes through the maximum of the meridional overturning streamfunction (the yellow dashed-dotted line in figure 3).

As shown in figure 2, the AMOC's northward branch winds around the gyres, following the red contours northward. The blue contours in figure 2 represent the gyres. We expect that the strength of the gyres is independent of the strength of AMOC at long

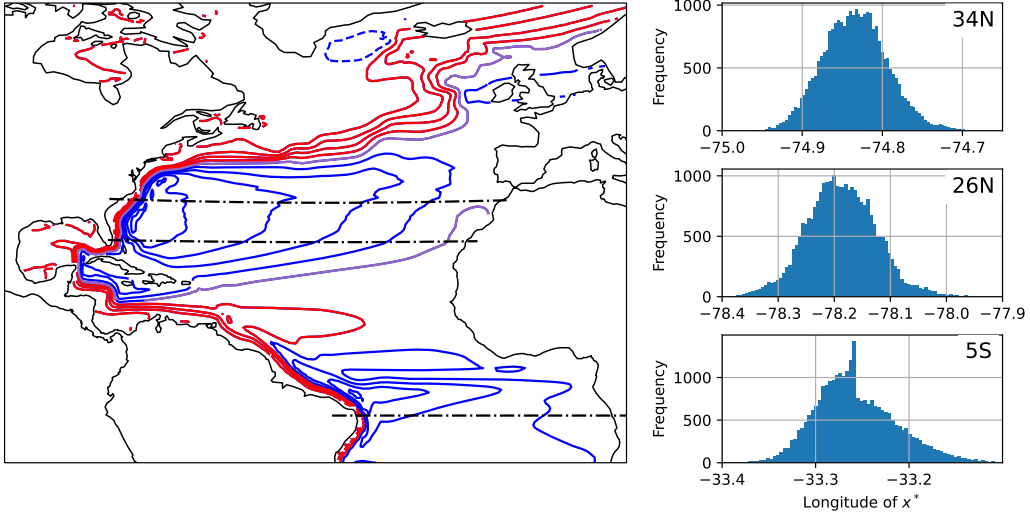


**Figure 2.** The red, blue and purple contours in the left panel show the pseudostreamfunction, the mean transport above  $\sigma_0 = 27.74$  (an isopycnal that passes through the maximum MOC streamfunction, as shown by the horizontal yellow line in figure 3) integrated from the western boundary eastward. The contour interval is 5 Sv. Red contours are contours that start in the south and end in the north, representing the AMOC. Blue contours are contours that cross each latitude twice, representing the gyres. The black dashed-dotted lines show the three latitudes used in this study. The right three panels are histograms of the location of  $x^*$ , the longitude that divides the AMOC transport and the gyre transport in the streamfunction splitting method (see the third panel of figure 1).

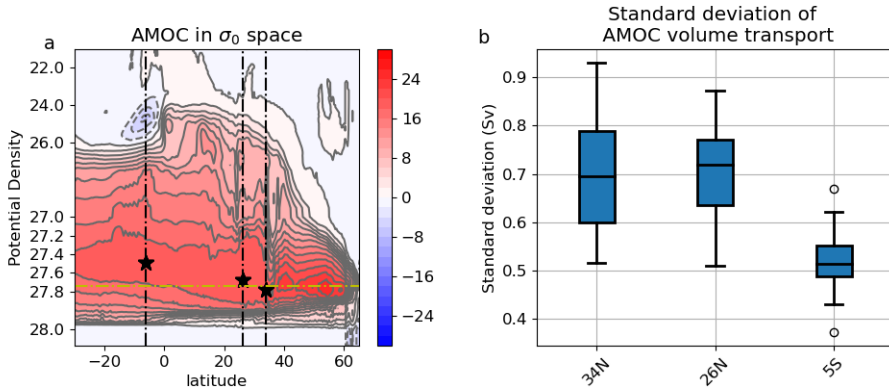


**Figure 3.** a) The Atlantic meridional overturning circulation in potential density space. b) The standard deviation of the AMOC volume transport at 34°N, 26°N and 5°S

208 timescales, and that the gyres are primarily driven by the wind, although recirculation  
 209 of northward AMOC transport may also be present.

210 Because the circulation is three-dimensional, the total transport above density sur-  
 211 face  $\rho_m$  contains a small divergent component, and  $\Phi$  is not a traditional streamfunc-  
 212 tion. A small number of open contours like the purple contour in figure 2 do not orig-  
 213 inate in the far south. These contours represent the movement of water that upwelled  
 214 across  $\rho_m$  within the domain.

215 In general, the red contours that represent the AMOC occupy the western bound-  
 216 ary only at latitudes with clockwise gyre circulation. In this paper, we focus on these  
 217 latitudes, because the AMOC pathway does not move around very much at these lat-  
 218 itudes. We plan to extend the method to other latitudes in future.

219 In our new method, which we call the streamfunction splitting method, a constant-  
 220 latitude section is divided into three regions. The first region is the deep region: this re-  
 221 gion is defined as the area below the dividing isopycnal, the green region in the bottom  
 222 panel of figure 1. This dividing isopycnal is chosen to be the isopycnal that passes through  
 223 the maximum of the meridional overturning streamfunction at that latitude (see stars  
 224 in figure 3a). The second region is the western-boundary region, the yellow region in the  
 225 bottom panel of figure 1, which is defined as the region above the dividing isopycnal and  
 226 west of the latitude  $x^*$ . Latitude  $x^*$  is chosen such that the volume transport through  
 227 the deep (green) region plus the volume transport through the western boundary (yel-  
 228 low) region sums to zero. The third region is the gyre region, the light blue region in the  
 229 bottom panel of figure 1, and this region is defined to be above the dividing isopycnal  
 230 and east of  $x^*$ . By definition, the volume transport through the gyre region is zero.

231 Here, we apply the streamfunction splitting method to the meridional velocity field  
 232 after performing a 24-month rolling time average in density space. Without this time-  
 233 average,  $x^*$  moves around a lot and sometimes is not defined. The dividing longitude  $x^*$   
 234 is shown in the right panels figure 2 at each latitude. Note that  $x^*$  is close to the west-  
 235 ern boundary in all cases, meaning that there is strong northward flow in the western  
 236 boundary current that is associated with AMOC.

237 Using a running mean that is applied after the heat transport is partitioned into  
 238 heat transport by the overturning and heat transport by the gyres, we further separate

239 the heat transport variability into variability on 2-10yr timescales and variability on 10+  
 240 year timescales. Ten years is chosen for ease of comparison with previous studies (e.g.  
 241 Larson et al. (2020)).

## 242 **3 Results**

### 243 **3.1 AMOC variability in the CESM large ensemble**

244 AMOC variability is one cause of inter-decadal heat transport variability. Figure  
 245 3a shows the mean MOC as a function of density in the CESM large ensemble: the depth  
 246 and mean strength of the MOC does not vary much between ensemble members. The  
 247 mean AMOC volume transport is about 20 Sv.

248 Figure 3a shows the standard deviation of the smoothed AMOC volume transport  
 249 at three different latitudes. The latitude  $34^{\circ}\text{N}$  is chosen because it is the most northerly  
 250 latitude before the Gulf Stream separates in observations. In CESM1, the Gulf Stream  
 251 separation latitude is further north than Cape Hatteras, but we have chosen to use  $34^{\circ}\text{N}$   
 252 because this is the most northerly latitude where the western boundary current compares  
 253 well with observations. The latitude  $26^{\circ}\text{N}$  is chosen because it is the location of the RAPID  
 254 array.  $34^{\circ}\text{N}$  and  $26^{\circ}\text{N}$  are relatively close together, and we expect the results at these  
 255 latitudes to be relatively similar.  $5^{\circ}\text{S}$  was chosen to examine AMOC transport variabil-  
 256 ity near to the equator. AMOC variability is generally larger at  $34^{\circ}\text{N}$  and  $26^{\circ}\text{N}$  than at  
 257  $5^{\circ}\text{S}$ , as shown in figure 3b, so we expect that AMOC-driven heat transport variability  
 258 will be larger at  $34^{\circ}\text{N}$  and  $26^{\circ}\text{N}$  than at  $5^{\circ}\text{S}$ .

### 259 **3.2 Heat transport variability in the CESM large ensemble**

260 Figure 4a-c shows the timeseries of heat and AMOC transport at the three cho-  
 261 sen latitudes for the third ensemble member, which is chosen as a representative ensem-  
 262 ble member. Heat transport is strongly correlated with AMOC at all three latitudes and  
 263 for both timescales of variability shown here (orange and blue lines in 4a-c).

264 Figure 4d-e shows the correlation between AMOC transport and heat transport  
 265 at the three chosen latitudes for all ensemble members, plotted as a function of the stan-  
 266 dard deviation of AMOC strength. Values further to the right have more AMOC vari-  
 267 ability and values further up have larger correlations between AMOC and AMOC heat  
 268 transport. Both AMOC variability and its correlation with heat transport are stronger

269 at 34°N and 26°N than at 5°S on 2-10yr timescales (figure 4d) and on 10+yr timescales  
 270 (figure 4e).

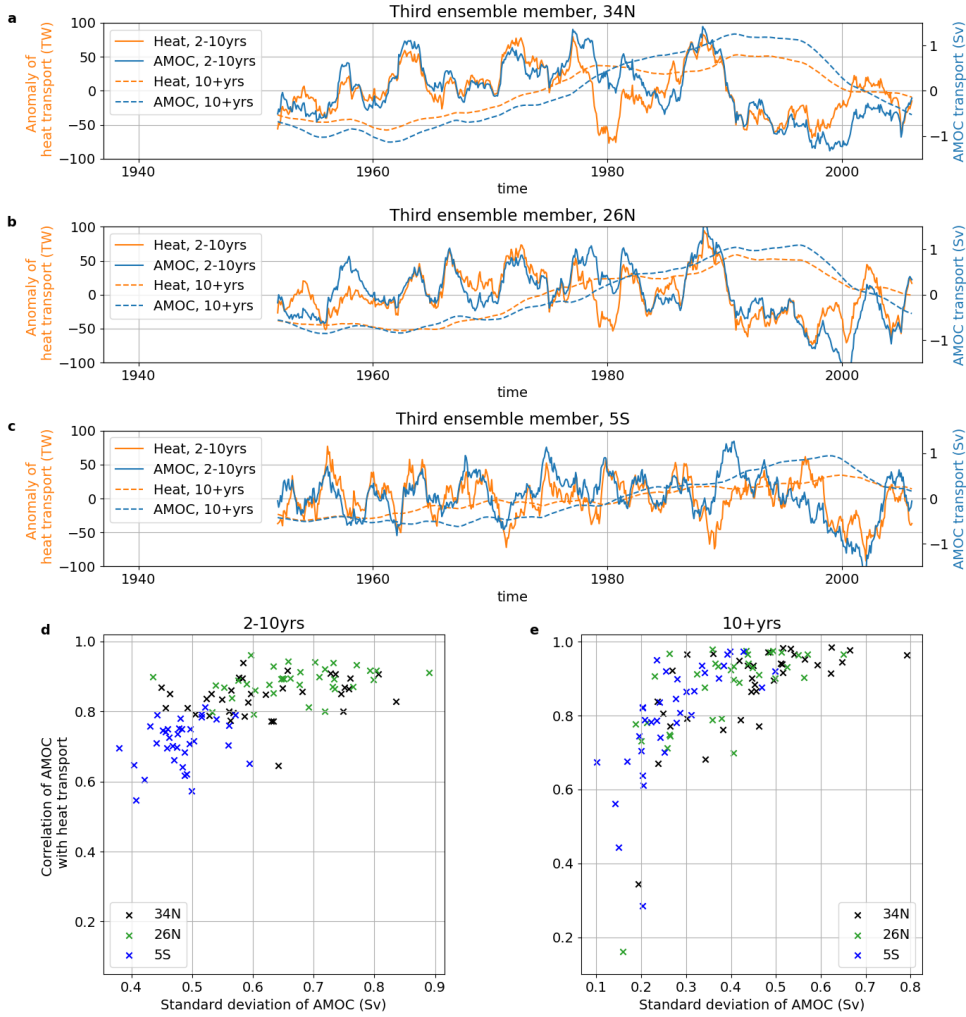


**Figure 4.** Timeseries of AMOC transport (blue) and heat transport (orange) for the third ensemble member, filtered to pick out variability on 2-10yr timescales (solid lines) and 10+yr timescales (dashed lines) at a) 34°N, b) 26°N and c) 5°S. The correlation between the smoothed heat transport and the smoothed AMOC transport at 34°N, 26°N and 5°S, plotted as a function of the standard deviation of the AMOC, filtered to pick out variability on d) 2-10yr timescales and e) 10+yr timescales (dashed lines). Each cross represents one ensemble member.

271 Most ensemble members show stronger correlations between AMOC and heat trans-  
 272 port at 10+yr timescales than at 2-10yr timescales, consistent with the idea that wind-  
 273 driven gyre variability is averaged out on timescales larger than 10 years. At all latitudes,

274 there are stronger correlations between AMOC and OHT in ensemble members with higher  
 275 AMOC variability.

276 Given the strong correlation between AMOC and OHT, it should be straightfor-  
 277 ward to decompose the component of OHT variability driven by AMOC variability. The  
 278 remainder of this work aims to elucidate the controls on heat transport at these differ-  
 279 ent latitudes and to compare methods for separating northward heat transport by the  
 280 gyres from northward heat transport by the overturning circulation.

### 281 **3.3 Heat transport by the gyres vs. heat transport by the overturning**

282 The mean meridional velocity in the first ensemble member at 34°N is shown in  
 283 figure 5a. The black contour indicates the mean depth of the isopycnal  $\rho_m$  and the hatched  
 284 region is the gyre region used in the streamfunction splitting method. The grey contour  
 285 indicates the topography. At this latitude, most of the northward flow in the western bound-  
 286 ary current is part of the AMOC. Southward flow at depth is not confined to the west-  
 287 ern boundary, but also occurs on the eastern flank of the mid-Atlantic ridge. The gyre  
 288 region contains both northward and southward velocities.

289 The heat transport at 34°N was separated into the heat transport by the net vol-  
 290 ume transport, the heat transport by the gyres and the heat transport by the overturn-  
 291 ing circulation using the three methods described in section 2.1. The results are plot-  
 292 ted in panels c and d of figure 5. All three methods give significantly different results.

293 In most ensemble members, the zonal-mean method in  $z$ -space attributes about 90%  
 294 of the heat transport to the overturning at 2-10 yr timescales (green box in figure 5c)  
 295 and at multidecadal timescales (green box in figure 5d), meaning that the gyre is respon-  
 296 sible for about 10% of the heat transport variability. Conceptual arguments suggest that  
 297 the zonal-mean method in  $z$ -space is likely to underestimate the heat transport variabil-  
 298 ity due to AMOC. In the zonal-mean method, the zonal mean temperature is multiplied  
 299 by the zonal integral of the velocity, even though most of the transport of the AMOC  
 300 follows the western boundary, where temperatures are much higher. At 34°N, the zonal  
 301 and depth mean temperature in the top 100m is about 20.2°C. West of 74.5°W (in the  
 302 western boundary where the AMOC is flowing northward), the zonal and depth mean  
 303 temperature in the top 100m is about 23.3°C. Hence we expect that the zonal-mean method  
 304 in  $z$ -space underestimates the heat transport variability due to AMOC at 34°N.

305 The zonal-mean method in density space attributes only about 45% of the heat trans-  
 306 port to the overturning on 2-10yr timescales and about 55% of the heat transport to the  
 307 overturning on 10+yr timescales. This is much lower than the other two methods, again  
 308 because AMOC variability mostly occurs on the western boundary at this latitude. Isopyc-  
 309 nals tilt upwards at the western boundary, and generally the water is warmer here. The  
 310 zonal average temperature in density space is much lower than the temperature on the  
 311 western boundary. As a result, the zonal-mean method in density space underestimates  
 312 the heat transport by the overturning even more than the zonal-mean method in  $z$ -space.

313 Our new method, which we call the western boundary splitting method, is not vul-  
 314 nerable to this problem. It attributes about 94% of the heat transport to the overturn-  
 315 ing in all ensemble members on 2-10yr timescales and about 120% of the heat transport  
 316 to the overturning on 10+yr timescales. More heat transport is attributed to AMOC than  
 317 one might expect based on the correlation between AMOC transport and the total heat  
 318 transport. The extra variability is compensated by heat transport attributed to the gyre,  
 319 which is anti-correlated with AMOC transport at 10+yr timescales.

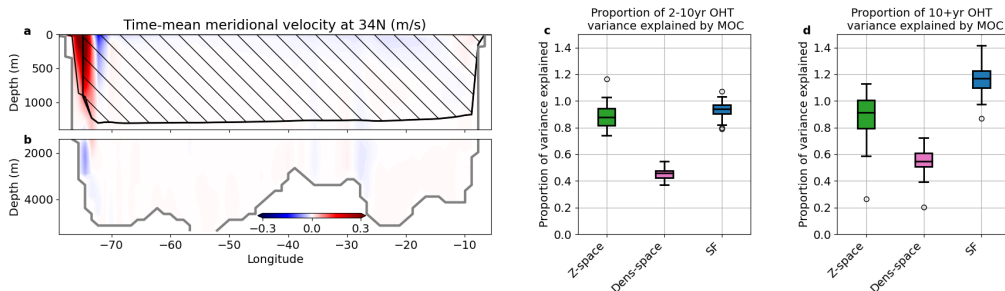


**Figure 5.** a and b show the time-mean meridional velocity at  $34^{\circ}\text{N}$  for the first ensemble member. The black contour shows the time-mean depth of the isopycnal that passes through the AMOC stream function's maximum. The hatched area is the area associated with the gyre in the streamfunction splitting method. The black vertical line shows the median location of  $x^*$ . c) A box and whisker plot of the heat transport on 2-10 yr timescales explained by each method, where the green box represents the proportion of variance explained by AMOC for the zonal-mean method in  $z$  space, the pink box represents the proportion of variance explained by AMOC for the zonal-mean method in density space, and the blue box represents the variance explained by AMOC for the streamfunction-splitting method. d) A box and whisker plot of the heat transport on 10+ yr timescales explained by each method (colors as in c).

320 At 26°N, both the zonal-mean method in  $z$ -space and the western boundary split-  
 321 ting method attribute about 100% of the heat transport variability to the AMOC on 2-  
 322 10yr timescales, while the zonal-mean method in density space attributes only 50% of  
 323 the heat transport to the AMOC (figure 6c). For the reasons described above, the zonal-  
 324 mean method in density space under-estimates the part of the heat transport that is per-  
 325 formed by the AMOC. On 10+yr timescales, the zonal-mean method in  $z$ -space again  
 326 attributes about 100% of the variability to AMOC, whereas the streamfunction split-  
 327 ting method attributes 120% of variability to AMOC, with some compensation between  
 328 the AMOC and gyres. Unlike other methods, it is clear what this compensation means  
 329 in the streamfunction splitting method. Times with high heat transport in the western  
 330 boundary are associated with times of low heat transport in the gyre region and vice versa.  
 331 This can easily be explained: when the AMOC transport is larger, more heat is trans-  
 332 ported northward and temperatures north of 26°N increase, reducing the difference in  
 333 temperature between northward and southward flowing water in the gyre region.

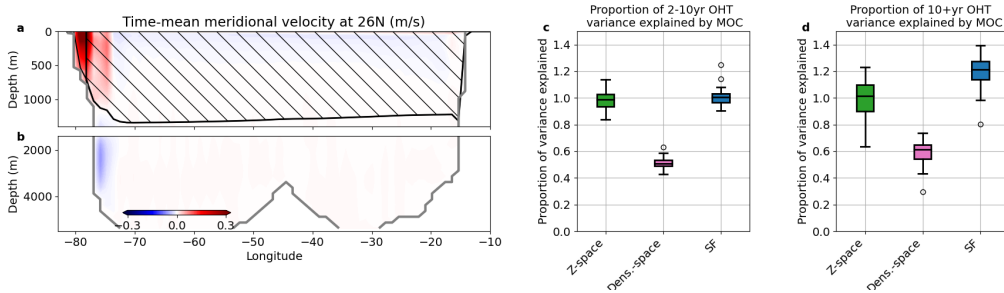


**Figure 6.** a and b show the time-mean meridional velocity at 26°N for the first ensemble member. The black contour shows the time-mean depth of the isopycnal that passes through the AMOC stream function’s maximum. The hatched area is the area associated with the gyre in the streamfunction splitting method. The black vertical line shows the median location of  $x^*$ . c) A box and whisker plot of the heat transport on 2-10 yr timescales explained by each method, where the green box represents the proportion of variance explained by AMOC for the zonal-mean method in  $z$  space, the pink box represents the proportion of variance explained by AMOC for the zonal-mean method in density space, and the blue box represents the variance explained by AMOC for the streamfunction-splitting method. d) A box and whisker plot of the heat transport on 10+ yr timescales explained by each method (colors as in c).

334 Because  $26^{\circ}\text{N}$  and  $34^{\circ}\text{N}$  are close together and both occur in the subtropical gyre,  
 335 we expect that heat transport by the overturning at  $26^{\circ}\text{N}$  and at  $34^{\circ}\text{N}$  are similar to each  
 336 other, particularly at long timescales. In figure 7, we plot the correlation between the  
 337 heat transport by the overturning at  $26^{\circ}\text{N}$  and at  $34^{\circ}\text{N}$  for the 2-10yr timescale and for  
 338 the 10+yr timescale. The zonal-mean method in density space and the streamfunction  
 339 splitting method both find strong correlations between ocean heat transport attributed  
 340 to overturning at  $26^{\circ}\text{N}$  and at  $34^{\circ}\text{N}$ , while the zonal-mean method in  $z$ -space generally  
 341 finds weaker correlations between the two latitudes. This is particularly obvious at 10+yr  
 342 timescales, for which the correlation between  $26^{\circ}\text{N}$  and at  $34^{\circ}\text{N}$  is close to one for the  
 343 streamfunction splitting method. This suggests that the zonal-mean method in  $z$ -space  
 344 is less robust than the other two methods, and may give different results even at sim-  
 345 ilar latitudes.

346 At  $5^{\circ}\text{S}$ , the zonal-mean method in  $z$ -space attributes about 85% of the heat trans-  
 347 port to AMOC on 2-10yr timescales (figure 8c). The zonal-mean method in density space  
 348 attributes less than 20% of the heat transport to AMOC, again suggesting that this method  
 349 severely underestimates the role of overturning in heat transport. The streamfunction  
 350 splitting method attributes about 55% of heat transport variability to AMOC. One rea-  
 351 son why the zonal-mean method in  $z$ -space and the streamfunction splitting method give  
 352 such different results is that the zonal-mean method in  $z$ -space counts the subtropical  
 353 cell in the overturning transport. The subtropical cell is primarily a vertical circulation  
 354 that comprises poleward flow very close to the surface and equatorward flow in the top  
 355 100m or so of the water column: because of the strong temperature contrast between these  
 356 two parts of the flow, the subtropical cell transports a lot of heat. The streamfunction  
 357 splitting method counts the most of the subtropical cell in the gyre transport, because  
 358 it takes place away from the western boundary.

359 At 10+yr timescales, the zonal-mean method in  $z$ -space and the streamfunction-  
 360 splitting method estimate that about 80% of heat transport variability is attributed to  
 361 the overturning (figure 8d). This is plausible, because the variability of the subtropical  
 362 cell generally has much shorter timescales. There is a wide variation between ensemble  
 363 members, possibly caused by low heat transport variability at this latitude on 10+yr timescales.  
 364 As above, the zonal-mean method in density space severely underestimates the role of  
 365 overturning in heat transport

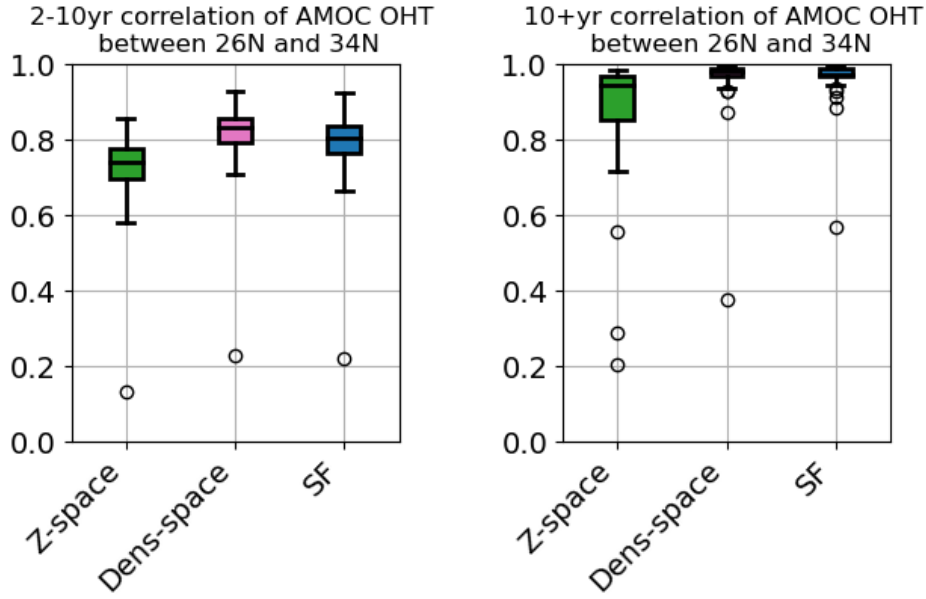


**Figure 7.** The left panel shows box and whisker plots of the correlation between the ocean heat transport attributed to AMOC at  $26^{\circ}\text{N}$  and at  $34^{\circ}\text{N}$  for each ensemble member, filtered to select 2-10yr timescales. The right panel shows the same, but filtered to select 10+ yr timescales. The green box represents the correlation between OHT explained by AMOC between  $26^{\circ}\text{N}$  and  $34^{\circ}\text{N}$  for the zonal-mean method in z space, the pink box represents the proportion of variance explained by AMOC for the zonal-mean method in density space, and the blue box represents the variance explained by AMOC for the streamfunction-splitting method

#### 366 4 Conclusions

367 In this paper, we present three methods for partitioning the AMOC heat transport  
 368 and the gyre heat transport in the Atlantic basin. The first two methods have been used  
 369 in the past: both methods estimate the heat transport by the AMOC using the prod-  
 370 uct of the zonal-mean temperature and the zonally-integrated volume transport. The  
 371 first method takes the zonal mean and zonal integral in depth space: we call this method  
 372 the zonal-mean method in z-space. The second method takes the zonal mean and zonal  
 373 integral in density space: we call this method the zonal-mean method in density-space.  
 374 The third method is a new method which uses physical information about the pathway

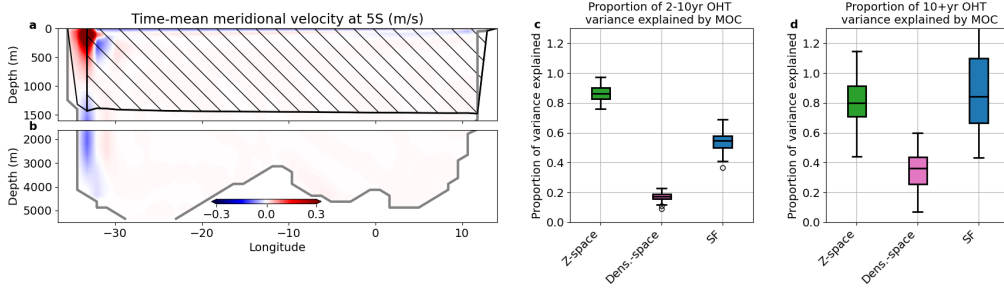


**Figure 8.** Total heat transport, heat transport by the net volume transport, heat transport by the overturning and heat transport by the gyres at  $5^{\circ}\text{S}$ , for a,c,e the third ensemble member and b,d,f the sixth ensemble member using a, b, the zonal-mean method in  $z$ -space, c, d, the zonal-mean method in density space, and e, f the western boundary splitting method. g) A box and whisker plot of the heat transport explained by each method.

375 of the AMOC to partition the two components of the heat transport. We call this method  
 376 the streamfunction splitting method.

377 We compare the methods at three different latitudes:  $34^{\circ}\text{N}$ ,  $26^{\circ}\text{N}$  and  $5^{\circ}\text{S}$ . At all  
 378 of these latitudes, the zonal-mean method in depth space and the zonal-mean method  
 379 in density space perform very differently from each other. The zonal-mean method in  
 380 in density space always attributes greater than 40% of heat transport to the gyre, and at  
 381  $5^{\circ}\text{S}$ , it attributes more than 70% of heat transport to the gyre. Given the strong cor-  
 382 relation between AMOC and heat transport at all three latitudes, it seems unlikely that  
 383 the gyre plays such a large role in heat transport. We find that the zonal-mean method  
 384 in density space is ineffective for partitioning the heat transport by the overturning and  
 385 the heat transport by the gyres.

386 The zonal-mean method in depth space and our new method sometimes give sim-  
 387 ilar results, but at  $34^{\circ}\text{N}$  and at  $26^{\circ}\text{N}$  the zonal-mean method in  $z$ -space indicates that  
 388 80% to 100% of multidecadal variability is explained by AMOC, with little compensa-  
 389 tion between the heat transport by the AMOC and the heat transport by the gyres. Like  
 390 the zonal-mean method in density space, the zonal-mean method in  $z$ -space underesti-  
 391 mates the heat transport variability due to AMOC because the zonally-integrated tem-  
 392 perature is smaller than the temperature of the northward-flowing AMOC transport. Our  
 393 new streamfunction-splitting method uses recent understanding of AMOC as a circula-  
 394 tion in density space, but also applies a new insight: that AMOC follows the western bound-

395 ary when it flows past clockwise gyre circulations. Hence, our new method does not use  
396 a zonal average and is not vulnerable to underestimating AMOC heat transport due to  
397 averaging over the whole width of the basin.

398 The new method presented here indicates that in CESM, heat transport by the AMOC  
399 explains about 120% of the multidecadal heat transport variability at 26°N and 34°N  
400 (with 20% compensated by southward heat transport in the gyre), and 80% of the heat  
401 transport variability at 5°S. Unlike the zonal-mean method in  $z$ -space, on long timescales  
402 our new method gives very similar results at latitudes that are close to each other. While  
403 our new method is difficult to apply directly to observations, it can be applied to any  
404 model and a long timeseries is not necessary.

405 At 5°S, the subtropical cell contributes to the vertical part of the meridional heat  
406 transport, but may or may not be considered part of the AMOC. Both the zonal-mean  
407 method in  $z$ -space and the streamfunction-splitting method are somewhat informative  
408 at this latitude: their differences highlight that much of the subtropical cell is found out-  
409 side the western boundary, and that the subtropical cell is a significant cause of heat trans-  
410 port variability on 2-10yr timescales. Future studies using Lagrangian particles could help  
411 elucidate how the subtropical cell and the upper cell of the AMOC are connected.

## 412 **5 Open Research**

413 The code repository for this paper is at [https://github.com/cspencerjones/amoc](https://github.com/cspencerjones/amoc_heat_code)  
414 [\\_heat\\_code](#). The data used in this research is the CESM1 Large Ensemble, which is hosted  
415 on Amazon Web Services (de La Beaujardiere et al., 2019). This work would not have  
416 been possible without the tools provided by and maintained by the Pangeo community  
417 (<https://pangeo.io/>).

## 418 **Acknowledgments**

419 Thanks to Navid Constantinou for several useful discussions about this work. CSJ's work  
420 on this project was supported by NSF award number OCE-2219852.

## 421 **References**

422 Bhagtani, D., Hogg, A. M., Holmes, R. M., & Constantinou, N. C. (2023). Surface  
423 heating steers planetary-scale ocean circulation. *Journal of Physical Oceanog-*

- 424            *raphy*.
- 425    Boccaletti, G., Ferrari, R., Adcroft, A., Ferreira, D., & Marshall, J. (2005). The ver-  
426            tical structure of ocean heat transport. *Geophysical Research Letters*, *32*(10).
- 427    Borchert, L. F., Müller, W. A., & Baehr, J. (2018). Atlantic ocean heat transport  
428            influences interannual-to-decadal surface temperature predictability in the  
429            north atlantic region. *Journal of Climate*, *31*(17), 6763–6782.
- 430    Bryan, K. (1962). Measurements of meridional heat transport by ocean currents.  
431            *Journal of Geophysical Research*, *67*(9), 3403–3414.
- 432    Buckley, M. W., & Marshall, J. (2016). Observations, inferences, and mechanisms  
433            of the Atlantic Meridional Overturning Circulation: A review. *Reviews of Geo-*  
434            *physics*, *54*(1), 5–63.
- 435    Cessi, P. (2018). The effect of Northern Hemisphere winds on the meridional over-  
436            turning circulation and stratification. *Journal of Physical Oceanography*,  
437            *48*(10), 2495–2506.
- 438    de La Beaujardiere, J., Banihirwe, A., Shih, C., Paul, K., & Hamman, J. (2019).  
439            NCAR CESM LENS cloud-optimized subset. *UCAR/NCAR Computational*  
440            *and Informations Systems Lab*. doi: 10.26024/wt24-5j82
- 441    Eden, C., & Willebrand, J. (2001). Mechanism of interannual to decadal variability  
442            of the North Atlantic circulation. *Journal of Climate*, *14*(10), 2266–2280.
- 443    Ferrari, R., & Ferreira, D. (2011). What processes drive the ocean heat transport?  
444            *Ocean Modelling*, *38*(3-4), 171–186.
- 445    Folland, C. K., Palmer, T. N., & Parker, D. E. (1986). Sahel rainfall and worldwide  
446            sea temperatures, 1901–85. *Nature*, *320*(6063), 602–607.
- 447    Foukal, N. P., & Chafik, L. (2022). The AMOC needs a universally-accepted defini-  
448            tion. *Authorea Preprints*.
- 449    Goldenberg, S. B., Landsea, C. W., Mestas-Nuñez, A. M., & Gray, W. M. (2001).  
450            The recent increase in Atlantic hurricane activity: Causes and implications.  
451            *Science*, *293*(5529), 474–479.
- 452    Gray, A. R., & Riser, S. C. (2014). A global analysis of Sverdrup balance using  
453            absolute geostrophic velocities from Argo. *Journal of Physical Oceanography*,  
454            *44*(4), 1213–1229.
- 455    Hall, M. M., & Bryden, H. L. (1982). Direct estimates and mechanisms of ocean  
456            heat transport. *Deep Sea Research Part A. Oceanographic Research Papers*,

457 29(3), 339–359.

458 Jackson, L., Kahana, R., Graham, T., Ringer, M., Woollings, T., Mecking, J., &  
459 Wood, R. (2015). Global and European climate impacts of a slowdown of the  
460 AMOC in a high resolution GCM. *Climate dynamics*, 45, 3299–3316.

461 Jones, C., & Cessi, P. (2018). Components of upper-ocean salt transport by the  
462 gyres and the meridional overturning circulation. *Journal of Physical Oceanog-*  
463 *raphy*, 48(10), 2445–2456.

464 Kang, S. M., Frierson, D. M., & Held, I. M. (2009). The tropical response to ex-  
465 tratropical thermal forcing in an idealized GCM: The importance of radiative  
466 feedbacks and convective parameterization. *Journal of the atmospheric sci-*  
467 *ences*, 66(9), 2812–2827.

468 Kay, J. E., Deser, C., Phillips, A., Mai, A., Hannay, C., Strand, G., . . . others  
469 (2015). The Community Earth System Model (CESM) large ensemble project:  
470 A community resource for studying climate change in the presence of internal  
471 climate variability. *Bulletin of the American Meteorological Society*, 96(8),  
472 1333–1349.

473 Klotzbach, P., Gray, W., & Fogarty, C. (2015). Active Atlantic hurricane era at its  
474 end? *Nature Geoscience*, 8(10), 737–738.

475 Larson, S. M., Buckley, M. W., & Clement, A. C. (2020). Extracting the buoyancy-  
476 driven Atlantic meridional overturning circulation. *Journal of Climate*, 33(11),  
477 4697–4714.

478 Marshall, J., Donohoe, A., Ferreira, D., & McGee, D. (2014). The ocean’s role in  
479 setting the mean position of the Inter-Tropical Convergence Zone. *Climate Dy-*  
480 *namics*, 42, 1967–1979.

481 Martin, E. R., & Thorncroft, C. D. (2014). The impact of the AMO on the West  
482 African monsoon annual cycle. *Quarterly Journal of the Royal Meteorological*  
483 *Society*, 140(678), 31–46.

484 McDonagh, E. L., McLeod, P., King, B. A., Bryden, H. L., & Valdés, S. T. (2010).  
485 Circulation, heat, and freshwater transport at 36 N in the Atlantic. *Journal of*  
486 *physical oceanography*, 40(12), 2661–2678.

487 Oldenburg, D., Wills, R. C., Armour, K. C., Thompson, L., & Jackson, L. C. (2021).  
488 Mechanisms of low-frequency variability in North Atlantic Ocean heat trans-  
489 port and AMOC. *Journal of Climate*, 34(12), 4733–4755.

- 490 Pickart, R. S., & Spall, M. A. (2007). Impact of Labrador Sea convection on  
491 the North Atlantic meridional overturning circulation. *Journal of Physical*  
492 *Oceanography*, *37*(9), 2207–2227.
- 493 Piecuch, C. G., Ponte, R. M., Little, C. M., Buckley, M. W., & Fukumori, I. (2017).  
494 Mechanisms underlying recent decadal changes in subpolar North Atlantic  
495 Ocean heat content. *Journal of Geophysical Research: Oceans*, *122*(9), 7181–  
496 7197.
- 497 Roemmich, D., & Wunsch, C. (1985). Two transatlantic sections: Meridional circula-  
498 tion and heat flux in the subtropical North Atlantic Ocean. *Deep Sea Research*  
499 *Part A. Oceanographic Research Papers*, *32*(6), 619–664.
- 500 Rypina, I. I., Pratt, L. J., & Lozier, M. S. (2011). Near-surface transport pathways  
501 in the North Atlantic Ocean: Looking for throughput from the subtropical to  
502 the subpolar gyre. *Journal of Physical Oceanography*, *41*(5), 911–925.
- 503 Stommel, H. (1957). A survey of ocean current theory. *Deep Sea Research (1953)*, *4*,  
504 149–184.
- 505 Talley, L. D. (1999). Some aspects of ocean heat transport by the shallow, inter-  
506 mediate and deep overturning circulations. *Geophysical Monograph-American*  
507 *Geophysical Union*, *112*, 1–22.
- 508 Trenberth, K. E., & Fasullo, J. T. (2017). Atlantic meridional heat transports com-  
509 puted from balancing earth’s energy locally. *Geophysical Research Letters*,  
510 *44*(4), 1919–1927.
- 511 Warren, B. A. (1999). Approximating the energy transport across oceanic sections.  
512 *Journal of Geophysical Research: Oceans*, *104*(C4), 7915–7919.
- 513 Yan, X., Zhang, R., & Knutson, T. R. (2018). Underestimated AMOC variability  
514 and implications for AMV and predictability in CMIP models. *Geophysical Re-*  
515 *search Letters*, *45*(9), 4319–4328.
- 516 Yang, J. (2015). Local and remote wind stress forcing of the seasonal variability of  
517 the Atlantic Meridional Overturning Circulation (AMOC) transport at 26.5 N.  
518 *Journal of Geophysical Research: Oceans*, *120*(4), 2488–2503.
- 519 Yeager, S. G., Karspeck, A. R., & Danabasoglu, G. (2015). Predicted slowdown in  
520 the rate of Atlantic sea ice loss. *Geophysical Research Letters*, *42*(24), 10–704.
- 521 Young, W. R. (2012). An exact thickness-weighted average formulation of the  
522 Boussinesq equations. *Journal of Physical Oceanography*, *42*(5), 692–707.

- 523 Zhang, R., Sutton, R., Danabasoglu, G., Kwon, Y.-O., Marsh, R., Yeager, S. G., . . .  
524 Little, C. M. (2019). A review of the role of the Atlantic meridional over-  
525 turning circulation in Atlantic multidecadal variability and associated climate  
526 impacts. *Reviews of Geophysics*, 57(2), 316–375.
- 527 Zhang, R., & Thomas, M. (2021). Horizontal circulation across density surfaces  
528 contributes substantially to the long-term mean northern Atlantic Meridional  
529 Overturning Circulation. *Communications Earth & Environment*, 2(1), 112.